Ore Geology Reviews 41 (2011) 49–74

Contents lists available at ScienceDirect

Ore Geology Reviews

journal homepage: www.elsevier.com/locate/oregeorev

Porphyry to epithermal transition in the Agua Rica polymetallic deposit, Catamarca, Argentina: An integrated petrologic analysis of ore and alteration parageneses

Marta Franchini [a,b,*], Agnes Impiccini [b], David Lentz [c], Francisco Javier Ríos [d], Sol O'Leary [a,b], Josefina Pons [a,b], Abel Isidoro Schalamuk [a,e]

[a] *Consejo Nacional de Investigaciones Científicas y Técnicas, Universidad Nacional del Comahue, Buenos Aires 1400, (8300) Neuquén, Argentina*
[b] *Centro Patagónico de Estudios Metalogenéticos, Facultad de Ingeniería, Universidad Nacional del Comahue, Buenos Aires 1400, (8300) Neuquén, Argentina*
[c] *Department of Geology, University of New Brunswick, Fredericton, NB, Canada*
[d] *CDTN/CNEN, Fluid Inclusion and Metallogenic Lab, Belo Horizonte, Brazil*
[e] *Instituto de Recursos Minerales, Facultad de Ciencias Naturales y Museo, Universidad Nacional de La Plata, La Plata, Argentina*

ARTICLE INFO

Article history:
Received 17 February 2011
Received in revised form 26 April 2011
Accepted 23 June 2011
Available online 1 July 2011

Keywords:
Porphyry
Epithermal
Polymetallic Cu–Mo–Au–Zn–Pb
High sulfidation
Neogene
Argentina

ABSTRACT

Agua Rica (27°26′S–66°16′O) is a world class Cu–Au–Mo deposit located in Catamarca, Argentina. In the E–W 6969400 section examined, the Seca Norte and the Trampeadero porphyries that have intruded the metasedimentary rock are cut by interfingered igneous and hydrothermal heterolithic and monolithic breccias, and sandy dikes. Relic biotite and K-feldspar of the early potassic alteration (370° to >550 °C) with Cu (Mo–Au) mineralization are locally preserved and encapsulated in a widespread, white mica + quartz + rutile or anatase halo (phyllic alteration) with pyrite + covellite that suggests fluids with temperatures ≤360 °C and high $f(S_2)$. The Trampeadero porphyry and the surrounding metasedimentary rock with phyllic alteration have molybdenite in stringers and B-type quartz veinlets and the highest Mo grades (>1000 ppm).

Multistage advanced argillic alteration overprinted the earlier stages. Early andalusite ± pyrite ± quartz is preserved in the roots of the argillic halo rimmed by an alumina–silica material and white micas. This alteration assemblage is considered to have been formed at temperatures ≥375 °C from condensed magmatic vapor. At higher levels, pyrophyllite replaces muscovite and illite in clasts of hydrothermal breccias in the center and east sector of the study section, suggesting temperatures of 280 to 360 °C. Clasts of vuggy silica in the uppermost levels of the central breccia, indicates that at lower temperatures (<250 °C), fluids reached very low pH (pH<2). In this early stage of the advanced argillic alteration, hydrothermal fluids seem to have not precipitated sulfides or sulfosalts.

Hydrothermal brecciation was concurrent with fluid exsolution (↑Δ V), which precipitated intermediate-temperature advanced argillic alunite (svanbergite + woodhouseite) ± diaspore ± zunyite as breccia cement along with abundant covellite + pyrite + enargite ± native sulfur ± kuramite at intermediate depths and in lateral transitional zones to unbrecciated rocks. This mineral assemblage indicates temperatures near 300 °C, oxidized and silica-undersaturated hydrothermal fluids with high sulfur fugacity to prevent gold precipitation. Multiple generations of pyrite, emplectite, colusite, Pb- and Bi-bearing sulfosalts, and native sulfur with Au and Ag, accompanied by alunite introduction in the upper level breccias, probably occurred at lower temperatures, but still high sulfur and oxygen activity. An independent Zn and Pb (as galena) mineralization stage locally coincides with Au–Ag and sulfosalts, and advanced at depth, controlled by fractures and overprinting much of the previous mineralization. A later paragenesis of veinlets of alunite + woodhouseite + svanvergite + pyrite ± enargite that cut the phyllic halo suggests temperatures ~250 °C and without woodhouseite + svanvergite, temperatures ~200 °C. Kaolinite occurs in the phyllic halo as a late mineral in clots and in veinlets thus, in this zone, the fluid had cooled enough for its formation.

1. Introduction

The Agua Rica porphyry-epithermal Cu–Au–Mo deposit is located in Catamarca province of Argentina, 25 km north of Andalgalá (27° 26′ S–66° 16′ W) and 15 km SW of Cerro Nevado del Candado (5450 m), the highest peak Sierra de Aconquija, one of the basement core uplifts of the Sierras Pampeanas. Compañía Cities Service Argentina S.A. initiated the first exploration (Koukharsky and Mirré, 1976; Navarro,

---

* Corresponding author at: Consejo Nacional de Investigaciones Científicas y Técnicas, Universidad Nacional del Comahue, Buenos Aires 1400, (8300) Neuquén, Argentina. Tel.: +54 299 4485344, 4488307; fax: +54 299 4485344.
E-mail address: mfranchi@uncoma.edu.ar (M. Franchini).

0169-1368/$ – see front matter © 2011 Elsevier B.V. All rights reserved.
doi:10.1016/j.oregeorev.2011.06.010

1986). Between 1994 and 1999, the deposit was explored in detail by a joint venture of BHP (Broken Hill Proprietary Limited) and Northern Orion Exploration Limited. A comprehensive report (BHP, 1999) of the lithology, alteration, mineralization, distribution of metals, and on the metallurgical ore types in the deposit was done, based on the results of 176 diamond drill holes, 2 tunnels, surface geology and in collaboration of academia with mapping surface breccia morphology and composition and sulfide mineralization and alteration. Agua Rica is a world-class Cu–Au–Mo deposit, soon to become a mine. It has an estimated resource total 797 Mt of 0.49% Cu, 0.23 g/t Au, 0.03% Mo, and 3.62 g/t Ag (Yamana Gold 2006, Feasibility Study Update; www.yamana.com). With the Bajo de la Alumbrera porphyry Cu–Au located 40 km west, they constitute the major Cu–Mo–Au resources of the Miocene Farallón Negro Volcanic Complex (Perelló et al., 1998; Sasso, 1997; Sasso and Clark, 1998).

The advance in the understanding of the Agua Rica deposit (BHP, 1999; Koukharsky and Mirré, 1976; Navarro, 1986; Perelló et al., 1998; Rojas et al., 1998; Rosco and Koukharsky, 1999; Sasso, 1997) and a detailed geologic map of breccia types have led Landtwing et al. (2002) to document a complex history of overprinting stages of subvolcanic intrusion, mineralization, brecciation, and erosion at Agua Rica; these authors summarized the following magmatic–hydrothermal stages: 1) the emplacement of the Melcho intrusions (8.6 to 6.3 Ma) at depth with associated subeconomic potassic and propylitic alteration and weak pyrite ± chalcopyrite ± molybdenite mineralization; 2) the emplacement and crystallization of the Seca Norte and Trampeadero feldspar porphyries associated with potassic alteration, intense quartz stockwork veining and chalcopyrite–molybdenite ± bornite mineralization (dated at 5 Ma); 3) magmatic fluid exsolution resulting in igneous breccias, melt fragmentation (locally tuffisitic), formation of hydrothermal breccias and subsequent advanced argillic and phyllic alteration types with sulfidation of earlier assemblages (cf. Burnham, 1985; Sillitoe, 1985), including previous sulfides, redistribution of the economic ore metals, precipitation of covellite–pyrite ± native sulfur, and addition of As (in enargite), Pb, Zn and locally higher grade Au zones (dated at 4 Ma); 4) phreatomagmatic eruption at shallow levels involving fragmentation of preexisting rocks and erupting melt and the input of juvenile magma with the formation of barren surface-venting crater infill breccia and a subsequent intrusion of a barren dacitic biotite porphyry dike. The supergene alteration and secondary enrichment of covellite were important and probably occurred while the actual drainage pattern was being established. These deep, intermediate and shallow events are now exposed at the same level of erosion. The telescoping was probably driven by the progressive degradation of the paleosurface (exhumation) due to regional uplift (and concomitant rapid erosion) (see Kesler and Wilkinson, 2006) of Sierras Pampeanas along NE-striking faults (Allmendinger, 1986; Bissig et al., 2001; Jordan and Allmendinger, 1986; Sasso, 1997; Sasso and Clark, 1998).

The present study brings, for the first time, a detailed description of the distribution of the hydrothermal alteration and mineralization and their minerals assemblages along the east–west main section of the Agua Rica deposit. The results precisely document the porphyry–epithermal transition at present described in only a few examples worldwide (i.e., Far Southwest: Hedenquist et al., 1998; Maricunga: Muntean and Einaudi, 2001; Tampakan: Rohrlach, 2003) and can be very useful for the mine development.

2. Regional geology

Agua Rica is located at the northern end of the Sierras Pampeanas geological province close to the southern margin of the Puna geological province (Fig. 1a), and separated by the NE-striking Tucumán Transfer Zone (Urreiztieta et al., 1993). The region has Paleozoic metamorphic and granitic rocks intruded by the Farallón Negro Volcanic Complex (FNVC) and a basin and range topography (Jordan and Allmendinger, 1986) developed in the Late Miocene (Sasso, 1997).

The Farallón Negro Volcanic Complex (12.56–5.16 Ma; Sasso, 1997; Sasso and Clark, 1998) is the easternmost manifestation of Neogene volcanic activity in this area, and constituted part of an extremely broad and scattered volcanic zone across the Andes (Clark et al., 1976). It lies within a transect in which the inclination of the present-day Wadati–Benioff Zone gradually decreases from north to south (Sasso, 1997; Sasso and Clark, 1998). The ascending magma may have been facilitated by the formation of local extensional basins along the Tucumán Transfer Zone (Sasso and Clark, 1998). The complex has long been considered to represent the remnants of a large stratocone hosting numerous subvolcanic intrusions, which was eroded to a sub-horizontal section through the base of the volcanic system (Caelles et al., 1971; Llambías, 1970, 1972). For Harris et al. (2006), the Farallón Negro succession is dominated by thick sequences of volcano-sedimentary breccias with only minor lavas deposited on an active foreland sedimentary basin to the Puna–Altiplano. Major extrusive events in the FNVC occurred between 9.7 and 7.35 Ma, with cogenetic porphyry intrusions emplaced between 8.3 and 6.1 Ma into the Farallón Negro andesite and farther east, into the Paleozoic basement, that are responsible in forming the porphyry Cu–Au Bajo de la Alumbrera (Ulrich et al., 2001; Ulrich and Heinrich, 2001) and the Agua Rica deposit (Koukharsky and Mirré, 1976; Perelló et al., 1998; Rojas et al., 1998). Other small deposits associated with the intrusive complex are the Capillitas epithermal polymetallic veins (Márquez-Zavalía, 1999; Márquez-Zavalía and Craig, 2004) and the Farallón Negro silver and gold veins (Llambías, 1970; Malvicini and Llambías, 1963).

Geochemical data for the magmatic rocks indicate that the evolution of the system was dominated by mixing of a mafic magma with a felsic magma that contained a component of crustal material. After 8.5 Ma, a continuous increase in the silica content of intrusive rocks suggests a combination of greater assimilation and (or) fractionation of this magmatic system episodically feeding into the magma chamber. A substantial magma reservoir ($>7\ \mathrm{km}^3$) must have been established to allow the rapid release of a large volume of ore-forming magmatic brine as a result of wholesale crystallization and devolatilization of the magma chamber (Halter et al., 2004).

Along the south margin of the low angle segment of the Benioff zone are located other Cenozoic Andean world-class porphyry Cu deposits, such as Pelambres, Pachón, Río Blanco, and El Teniente (Fig. 1a). Thus, as it was suggested by Proffett (2003), the space–time location along magmatic arcs for Agua Rica, Bajo de la Alumbera, and these porphyry Cu deposits may be associated with a flat slab subduction regime.

3. Material and methods

Seventy two samples of hydrothermally altered rocks were collected from 4 BHP drill cores. Fig. 1c shows drill hole locations in the east–west section 6969400 N across the Agua Rica deposit. Textures and phyllosilicate relationships were analyzed first in drill cores with a binocular microscope and then petrographically. Following Seedorff and Einaudi (2004), minerals in an assemblage (minerals in contact which appear stable and contemporaneous) are enumerated and separated by the plus symbol (+) and the plus or minus symbol (±). When a group of minerals characteristic of a certain alteration are not necessarily contemporaneous, they are separated by commas.

X-ray diffraction (XRD): The minerals were identified using a Rigaku DMAX-2D diffractometer at the Centro de Investigaciones en Minerales Arcillosos de la Universidad Nacional del Comahue, Neuquén. Bulk samples and the clay fraction ($<2\ \mu\mathrm{m}$) were analyzed from 2° to 40° 2θ, at 2° 2/min, with CuK alpha radiation, run at 40 kV and 20 mA. The XRD reflections were evaluated with Rigaku software. For all samples, clay identifications were by XRD of the 2 μm fraction

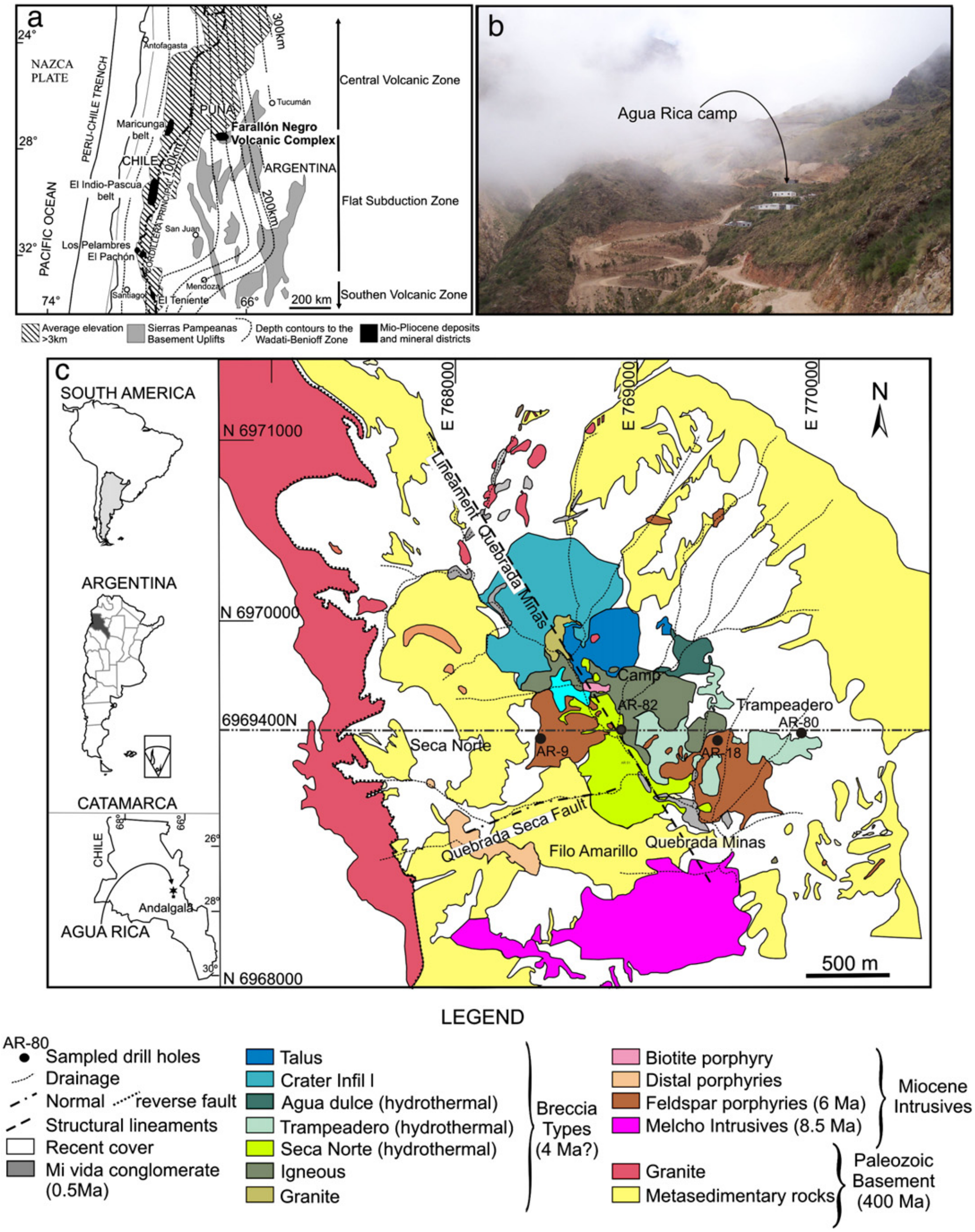

Fig. 1. a) Location of the Farallón Negro Volcanic Complex within the framework of the Andes convergent margin (modified from Bissig et al., 2002 and reference therein). b) View of the Agua Rica camp. c) Geological map of the Agua Rica district with the location of the E-O6969400 N cross section and sampled drill holes (modified from BHP, 1999 and Landtwing et al., 2002).

as oriented aggregates. Whole-rock samples (each corresponding to half pieces of drill core approximately 8 cm long and 2 cm thick) were crushed and ground with a mortar and pestle and then 30 g of each powdered whole rock were added to 1 l of distilled water and dispersed by ultrasonic probe. The <2 μm fraction was separated by timed centrifugation. Oriented preparations of Sr-saturated <2 μm fraction were analyzed by means of XRD in air-dried (AD) state (drying at room condition), ethylene glycol (EG) solvation, and heating to 375 °C and 550 °C for 1 h. The quantitative clay analyses were carried out using the Mineral Intensity Factor (MIF) method described in Moore and Reynolds (1997).

Chemical composition of minerals: mineral compositions were determined by electron microprobe analyses (EPMA) (n = 300) at the Microanalytical facility at the University of New Brunswick (Canada); mineral compositions were determined in wavelength-dispersion mode on a JXA JEOL-733 Superprobe, with 15 kV accelerating voltage, 10 nA beam current, and a maximum 40 s counting interval. The beam size was set to be 5 μm. A combination of various mineral and metal standards was used with ZAF matrix corrections by means of CITZAF version 3.03 (J.T. Armstrong, 1997, shareware; Division of Earth and Planetary Sciences, the California Institute of Technology). The analytical limits are on the order of 0.05 wt.%. Further EPMA (n = 81) were obtained from the Laboratorio de Microanálisis del Departamento de Física, Universidade Federal de Minas Gerais, Belo Horizonte, Brazil, using a Jeol-JXA-8900 RL WD/ED with 15 kV accelerating voltage, 20 nA beam current, and a 10 s counting interval in the peak and 5 s in both sides of the background. A combination of various mineral and metal standards was used with ZAF matrix corrections by means of JEOL software. The analytical limits are on the order of 0.05 wt.%.

Fluid inclusions: fluid inclusions and textural analyses in this study were conducted on quartz samples of Agua Rica at the Fluid Inclusion and Metallogeny Laboratory (LIFM) of the Centro de Desenvolvimento de Tecnología Nuclear (CDTN), Belo Horizonte, Brazil, using a Fluid Inc and a Linkam IR heating/freezing system stage adapted to a Leica DMR-XP microscope and the methodology detailed in Rosiére and Rios (2004) and Rios et al. (2006). For calibration and precision tests commercially available synthetic standards were used. The microscope is equipped with a 100 W (12 V) transmitted-light illuminator using halogen light bulbs as a source of visible and very near infrared radiation. The doubly polished sections studied of Agua Rica were about 80 to 100 μm thick. A Sony ExwaveHad black and white, very near-IR camera and an Eletrophysics Micronviewer Model 7290-A IR camera, both coupled to a high-resolution monitor with a video graphic printer, provided the normal and infrared images.

4. Deposit geology

The Agua Rica deposit is localized in the Sierra del Aconquija, one of the uplift blocks of the Sierras Pampeanas basement, 200 km east of the Cordillera de los Andes (Fig. 1a). The area is dissected by deep V-shaped valleys and continues to be eroded. Unconsolidated sediments partially cover the topography. The oldest rocks in the region consist of Precambrian or Early Paleozoic massive to laminated meta-quartz arenite, meta-subarkose, hornfels, phyllite, schist, and quartzite belonging to the regional greenschist facies metamorphism (Fig. 1c) (Koukharsky and Mirré, 1976). In sectors they are cut by metamorphic quartz veins up to 1 m in width. These metamorphic rocks were folded in a large open structure with a vertical axial plane that strikes SSE–NNW. Paleozoic granitic plutons and pegmatites (422.7 ± 6.1 and 438.4 ± 6.3 Ma, K–Ar muscovite ages; Capillitas–Belén granite suite; Caelles et al., 1971; Koukharsky and Mirré, 1976) intrude the metasedimentary rocks (Fig. 1c).

During the Miocene, a series of porphyritic stocks intruded the country rocks (Navarro, 1986; Perelló et al., 1998; Sasso 1997; Sasso and Clark, 1998). The earliest porphyries, called the Melcho Intrusive Complex, outcrop south of the deposit (Fig. 1c) and their emplacement have been dated at 8.56 ± 0.48 Ma (Ar–Ar age in hornblende; Sasso, 1997; Sasso and Clark, 1998). Four variants have been recognized (BHP, 1999): (1) equigranular to strongly porphyritic amphibole–feldspar porphyry with plagioclase, amphibole, and K-feldspar phenocrysts; (2) equigranular to weakly porphyritic amphibole–quartz–plagioclase porphyry with phenocrysts of plagioclase, quartz, and amphibole; (3) moderate to strongly porphyritic quartz–feldspar porphyry with plagioclase, quartz, and minor biotite and amphibole phenocrysts, and (4) equigranular quartz–feldspar intrusion with plagioclase, quartz, and minor biotite and amphibole phenocrysts. The latter two variants are associated with porphyry-style stockwork veining, potassic and propylitic alteration with disseminated Cu–Mo–Au mineralization (BHP, 1999). Two irregular bodies of feldspar porphyry host the porphyry Cu (Mo) type mineralization: the Trampeadero in the east and the Seca Norte in the west (Fig. 1c). Contacts between these porphyries and country rocks are sharp and vertical. The Trampeadero porphyry has preserved its intrusive contacts with the metasedimentary country rocks east and south and with the Seca Norte porphyry to the west, but most of the contacts are brecciated (Fig. 1c). The K–Ar dating of hydrothermal biotite in altered Seca Norte porphyry yielded an age of 5.10 ± 0.05 Ma (Perelló et al., 1998) and a trachyandesite (monzonite) composition was inferred for both porphyries (see BHP, 1999). Significant variations in their texture suggest multiple intrusive facies (Landtwing, 1998; Perelló et al., 1998). Two main variants have been determined (BHP, 1999): (1) medium- to coarse-grained, porphyritic feldspar porphyry is the dominant with zoned plagioclase, biotite, amphibole, minor quartz phenocrysts, and scattered, large K-feldspar phenocrysts in a fine-grained quartz–feldspar groundmass, and (2) fine-grained, porphyritic, mafic feldspar porphyry, with plagioclase, amphibole, biotite, and quartz phenocrysts. Based on major-element classification (BHP, 1999), the igneous rocks at Agua Rica are calc-alkaline with high K content, similar to the Farallón Negro igneous complex (Sasso, 1997). Immobile trace-element characterization indicates they are alkaline and were derived from a common parent magma (BHP, 1999).

Landtwing et al. (2002) mapped and described outcrops of various breccia types in the Agua Rica district (Fig. 1c). Based on these authors' research results, the volumetrically most prominent is a hydrothermal breccia that is exposed south and southeast of the Agua Rica camp, along the Quebrada Minas lineament (Fig. 1c). An igneous breccia (Fig. 1) with clasts (5–30 vol.%) of metasedimentary rocks and feldspar porphyry set in a fine-grained porphyritic igneous matrix is interfingered with the hydrothermal breccia. A matrix-supported and bedded crater infill breccia occupies a circular area in the northern part of the Agua Rica prospect (Fig. 1). A granite breccia with 90% unmineralized granitic material (Pabellón granite and pegmatites) outcrops in the center of the prospect (Fig. 1). A clast-supported, monomictic and unmineralized talus breccia outcrops north of the Agua Rica camp (Fig. 1) and overlies early breccias and metasedimentary rocks. Several small porphyritic bodies have been mapped along the margin of the deposit (distal porphyries; Landtwing et al., 2002) and a dike of unmineralized biotite porphyry outcrops near the Agua Rica camp (Fig. 1c). The porphyries and breccias were emplaced along the SE-striking Quebrada Minas lineament (Fig. 1c). East–west striking, south-dipping normal faults were active both syn- and post-mineralization. The Quebrada Seca fault (Fig. 1c) offsets leached material, and hydrothermal fluids from the high sulfidation, epithermal event were focused along the same structure. The Agua Rica camp structure has the same orientation as the Quebrada Seca fault and may have controlled emplacement of the biotite porphyry (Fig. 1c). West–southwest dipping low-angle reverse faults (Fig. 1c) have structurally thickened the leached capping on the west side of the deposit; the thrusted granite–metasedimentary rock contact has this same geometry (see Landtwing et al., 2002).

5. Geology of the E–W section along 6969400m

An E–W section (6969400 N) of the Agua Rica deposit through the most important mineralized bodies was selected for this study. The geology of this critical section (Fig. 2a) consists of massive to laminated metasedimentary wallrock to the Seca Norte (west) and the Trampeadero (east) feldspar porphyries separated by the Quebrada Minas hydrothermal breccia pipe and the igneous breccia (center of the section, in the base of the hydrothermal breccias). The hydrothermal breccia continues east, affecting the upper levels of the Trampeadero porphyry and the metasedimentary rocks. Steeply dipping normal structures may have offset these units. From west to east the selected drill holes that cut the mineralized units are the following: AR-9 (Seca Norte feldspar porphyry), AR-82 (hydrothermal breccias and metasedimentary rock), AR-18 (Trampeadero feldspar porphyry and hydrothermal breccia), and AR-80 (metasedimentary rock and hydrothermal breccia) (Fig. 2a). This study proposes a modification to the earlier interpretation of the geology of the section (see Landtwing et al., 2002): below 333 m the AR-82 drill hole intercepts the altered metasedimentary rock locally intruded by thin porphyry dikes, instead of the Seca Norte porphyry.

6. Alteration in the E–W section along 6969400m

6.1. Potassic alteration

From all studied samples, remnants of potassic alteration with hydrothermal biotite and K-feldspar is present only as patches in the

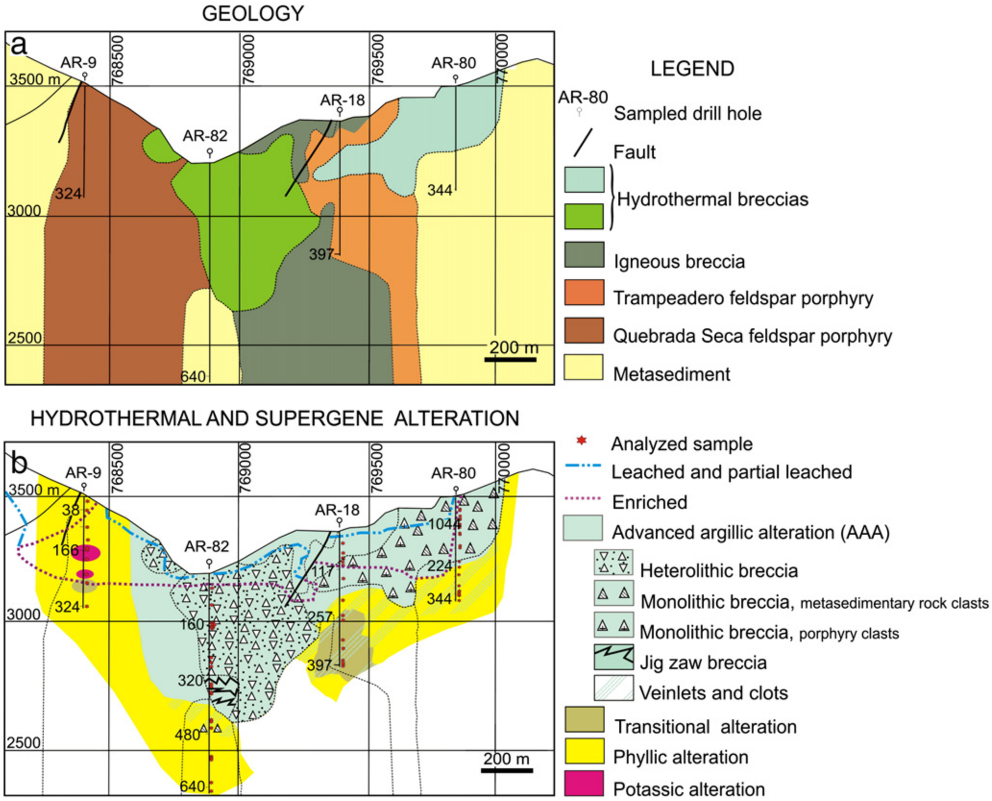

Fig. 2. a) Geology of the E–O section along 6969400 N with the location of sampled drill holes and analyzed samples (modified from BHP, 1999). b) Lateral and vertical distribution of hydrothermal and supergene alteration types along the section.

Seca Norte porphyry at 166, 187.7, and 223 m depth in drill hole AR-9 (Fig. 2b). In these samples, the porphyritic texture of the rock is partially preserved with cloudy hydrothermal K-feldspar phenocrysts replaced by white micas and rimmed by sulfides, with rare relict quartz phenocrysts and phenoclasts hosted in a silicified tuffisitic groundmass (Fig. 9). The hydrothermal biotite occurs at 166 and 223 m depth, as very fine brownish plates (from 0.05 to 0.3 mm) in aggregates replacing primary ferromagnesian silicates (amphibole and biotite), and are interconnected by irregular biotite replacement veinlets commonly described as stringers. In contact with sulfides, biotite is altered to white mica + rutile or anatase. At 187.7 m depth, pervasive hydrothermal K-feldspar alteration occurs instead of biotite.

6.2. Phyllic alteration

In this section phyllic alteration occurs as an envelope to the above and centrally located zone of advanced argillic alteration (Fig. 2b). The Seca Norte (drill hole AR-9) and Trampeadero (drill hole AR-18) porphyries host a pervasive, dominantly white mica assemblage with stockwork quartz veining. Patches or clots of phyllosilicates rimmed or intergrown with sulfides present a distinctive outline in a dominantly silicified groundmass, masking the original porphyritic texture (Fig. 9); some samples preserved a few intensely fractured quartz phenocrysts. White micas appear as very fine (<0.01 mm) grains associated with very fine-grained rutile or anatase, and rare small anhedral quartz in clusters that selectively replace (pseudomorph) phenocrysts of early hydrothermal biotite and K-feldspar; locally white micas occur as coarser grained sheets (up to 0.8 mm long) in radiating fibrous aggregates. A polycrystalline fine-grained quartz aggregate extensively replaces the groundmass of these porphyries. When compared with Seca Norte alteration (AR-9), the Trampeadero porphyry (AR-18) preserved the phyllic alteration in deeper zones (from 167 m below the surface), but was overprinted by advanced argillic alteration veinlets and clots (Fig. 9); the phyllosilicate clots are smaller, and rutile or anatase crystals are larger and more abundant. A similar phyllic alteration assemblage to the porphyries has been intersected in the metasedimentary rock by drill holes AR-82 and AR-80 below 480 and 227 m, respectively. Texture varies from fine-grained disseminations to alternating seams of phyllosilicates + sulfides + rutile or anatase with quartz bands and segregations preserving the metamorphic lamination and veins (Fig. 9).

6.3. Quartz veinlets

Irregular quartz veinlets of 0.2 to about 1 cm thick, with no matching walls and lack of internal symmetry (Fig. 9), were found only in the Seca Norte porphyry. Vein quartz has vitreous luster, pinkish gray color, anhedral granular texture, with crenulated borders and locally exhibits deformation. They are similar to early A-type veins (Gustafson and Hunt, 1975) of porphyry Cu deposits formed at least in part by replacement of wall rock, but without their typical mineral assemblage; they are cut by numerous biotite or sulfides along hairline veinlets (Fig. 9). Widespread veinlets with parallel walls filled with imperfect prismatic crystals of quartz occur in porphyries and metasedimentary rock with phyllic alteration. They lack deformation and are locally intergrown with sulfides and phyllosilicates (Fig. 9); they resemble B-type veins (Gustafson and Hunt 1975). These veinlets can be leached of sulfides or reopened by vein minerals deposited during later events (Fig. 9).

6.4. Transitional alteration

Clots of andalusite ± sulfides ± quartz in a white mica-rich assemblage has been locally preserved. Drill hole AR-9 at 264 m depth intercepts a zone in the Seca Norte porphyry with dominant phyllic alteration that contains scarce prismatic aggregates of andalusite intergrown with pyrite (which contains blebs of chalcopyrite); andalusite is rimmed and partially replaced by white mica

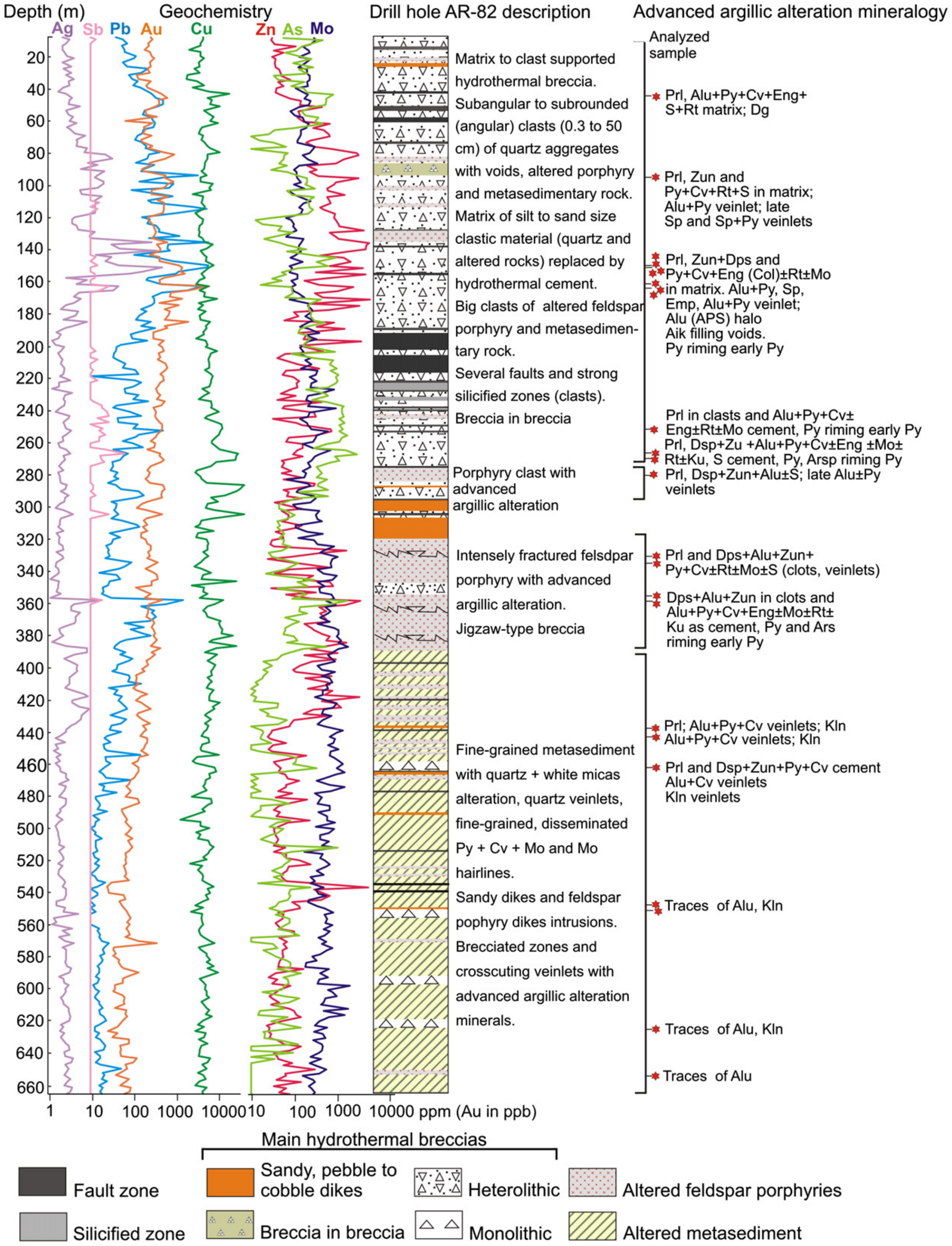

Fig. 3. Geochemistry, geology, alteration, and mineralogy of the advanced argillic alteration cut by drill hole AR-82 in the N 6969400 section. Data based on BHP (1999) and this contribution. Aik = aikinite; Alu = alunite; APS = woodhouseite, svanbergite; Ars = arsenopyrite; Bar = barite; Ccp = chalcopyrite; Cv = covellite; Col = colusite; Dg = digenite; Dsp = diaspore; Emp = emplectite; Eng = enargite; Gal = galena; Kln = Kaolinite; Ku = kuramite; Mo = molybdenite; Rt = rutile or anatase; S = native sulfur; Sp = sphalerite; Py = pyrite; Prl = pyrophyllite; and Zun = zunyite.

that also has an intergrown submicroscopic, cloudy alumina–silica material with 37.27 wt.% SiO_2, 30.88 wt.% Al_2O_3, and very low total (68.83 wt.%; microprobe results) reflecting its hydrous nature, which mantles corroded andalusite crystals (Fig. 10). Relict alkali feldspar has been identified in interstices between andalusite crystals. Andalusite is volumetrically more abundant in samples of the Trampeadero porphyry with dominant phyllic alteration (AR-18 at 248, 266.5, 347, and 382 m depth; Figs. 2b and 5), whereas it occurs

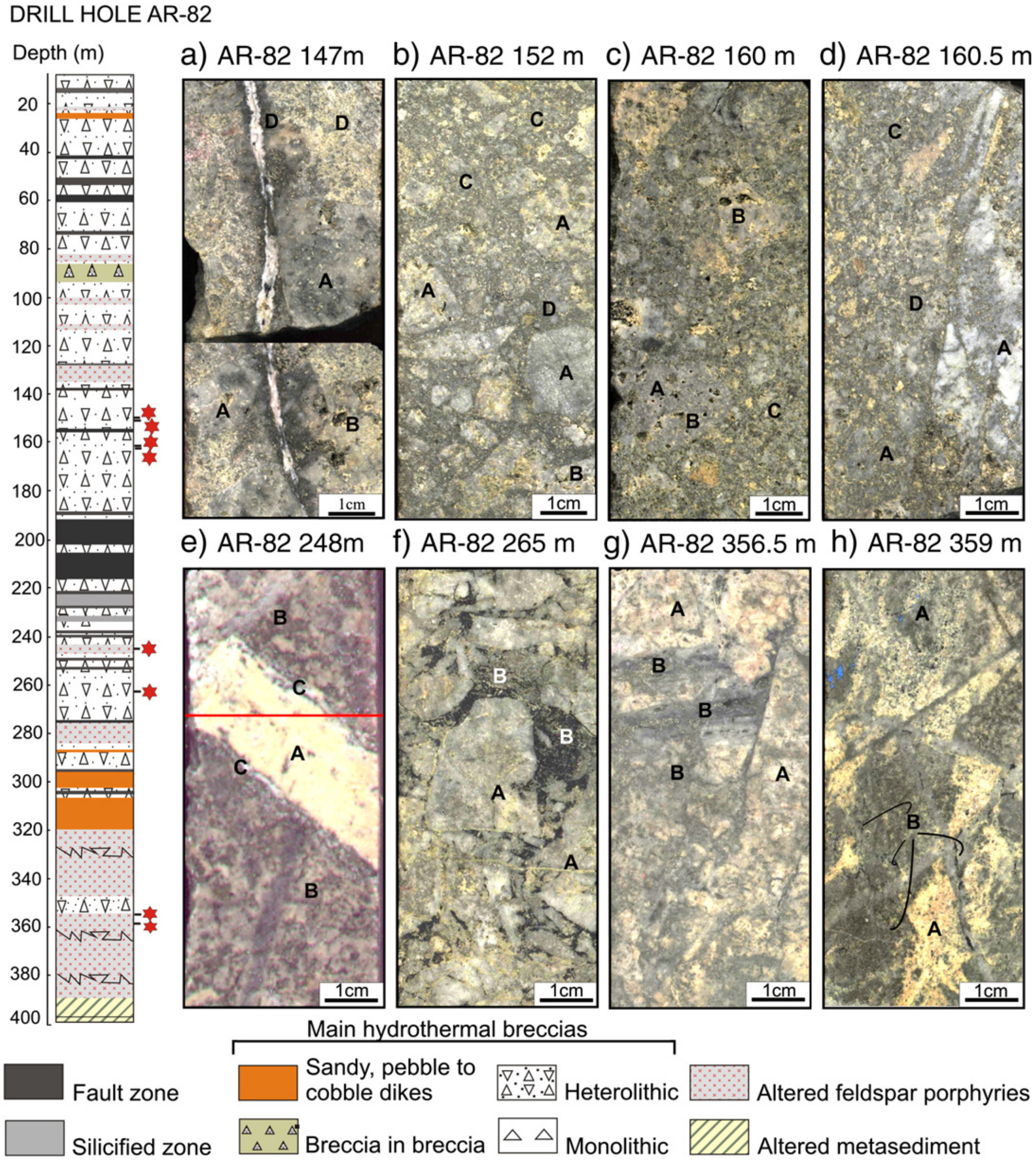

Fig. 4. Photographs illustrating different breccias types and hydrothermal infill of the advanced argillic alteration–mineralization stage cut by drill hole AR-82. a) to d): Matrix-supported heterolithc hydrothermal breccia. Clast are mainly residual quartz aggregates A with vugy texture B inserted in a fine-grained matrix of quartz and altered rock fragments C with hydrothermal infill D (alunite, zunyite, diaspore, various generations of pyrite, emplectite, aikinite, sphalerite, covellite, Au and Ag). Late veinlets and fractures cut the breccia (e.g. alunite + pyrite veinlet at a or fracture at c). e): Pyrophyllite veinlet A cut a boulder of altered porphyry B; the veinlet has been re-opened and filled with alunite that also forms a selvage with sulfides C. f): Clast supported hydrothermal breccia with altered porphyry clasts A and hydrothermal infill dominated by covellite + pyrite + enargite + alunite with diaspore + zunyite B. g) and h): Intensely fractured and altered porphyry with quartz veinlets A invaded by hydrothermal infill B, similar to a jigsaw breccia.

alone or with quartz and sulfides. Andalusite crystals have corroded margins and white mica rims (Fig. 10).

6.5. Advanced argillic alteration

At the scale of the entire deposit, advanced argillic alteration occurs as a keel or trough that trends north–south along the Quebrada Minas (Fig. 1) and from a minimum elevation of 2500 m to the surface, 800 m vertically. At 3000 m elevation, it covers an area of 800 × 1000 m. It is not limited to structural zones and does not occur at higher elevation within the porphyry style alteration–mineralization, as is common in other high sulfidation, advanced argillic altered porphyry systems (BHP, 1999).

In the section examined, this alteration type is centered in the Seca Norte hydrothermal breccias (drill hole AR-82) and extends to the east, affecting the hydrothermal breccias of the Trampeadero porphyry (drill hole AR-18) and the metasedimentary rock (drill hole AR-80); it is less prevalent in the unbrecciated Trampeadero porphyry and the metasedimentary rocks (Fig. 2b). A sharp and steep contact with phyllic alteration in the Seca Norte porphyry limits this alteration to the west (Fig. 2b). This bleeding of the AAA to the east has been attributed to result from hydrothermal fluids circulation along low angle, west dipping structures (BHP, 1999). It is characterized by the presence of pyrophyllite, alunite, diaspore, zunyite, and native sulfur as the most abundant minerals. Based on the textures and the mineral relations in the hydrothermal breccias, pre-brecciation and post-brecciation advanced argillic alteration stages were recognized. Nevertheless, the superposition of different epithermal stages on the early porphyry system makes the description of the temporal distribution of this assemblage challenging.

6.5.1. Pre-brecciation stage

In the heterolithic hydrothermal breccias (AR-82; Figs. 3 and 4), pyrophyllite occurs in clots and veinlets within fragments surrounded

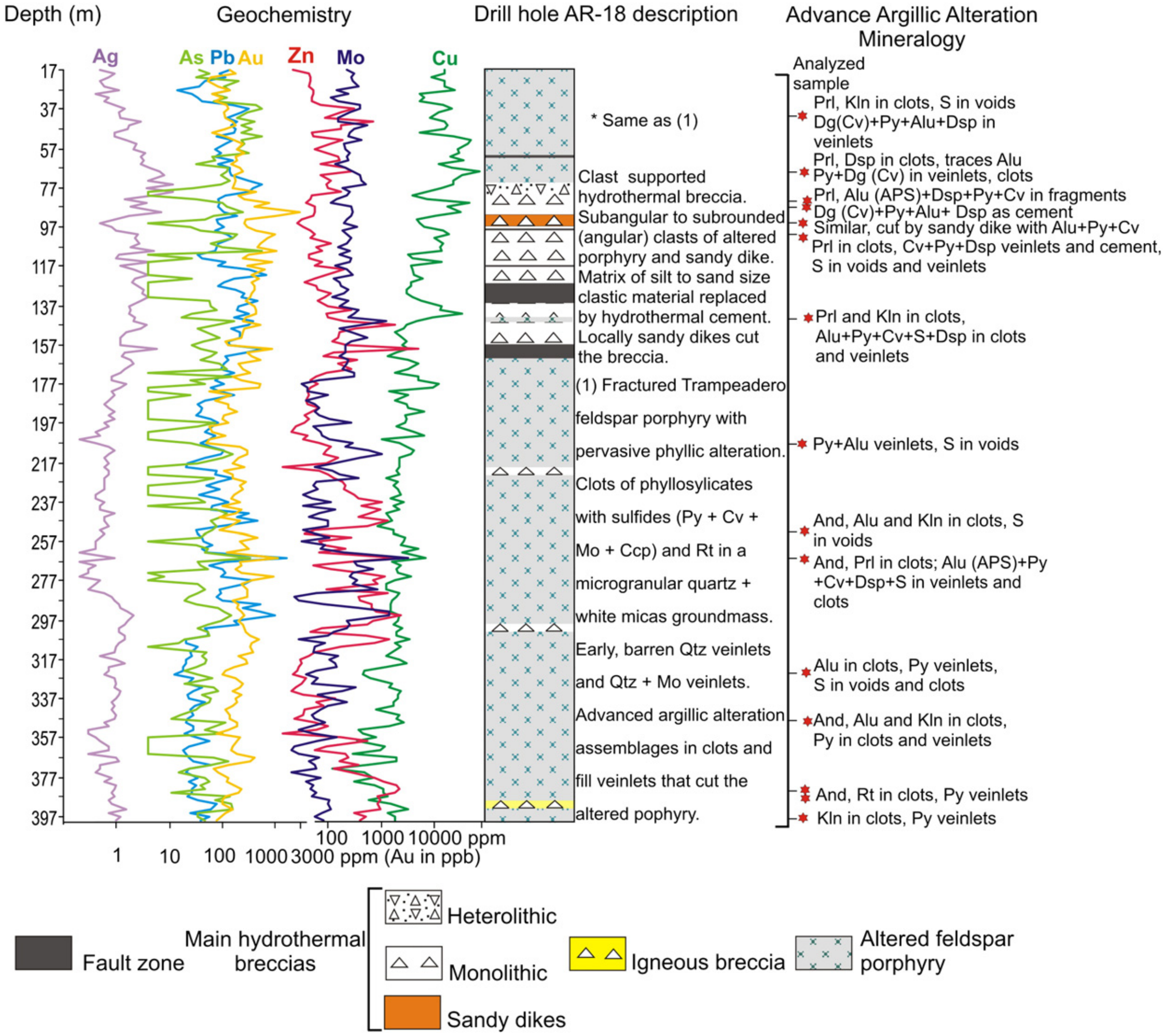

Fig. 5. Geochemistry, geology, alteration types, and mineralogy of the advanced argillic alteration cut by drill hole AR-18 in the N 6969400 section. Data based on BHP (1999) and this contribution. See explanation of symbols in Fig. 3.

by microcrystalline quartz aggregates and in the clastic matrix with a turbid appearance. In the Trampeadero monolithic hydrothermal breccia (drill hole AR-18, between 77 and 157 m, at 220, and at 300 m depth; Figs. 5 and 6), clasts of the feldspar porphyry have preserved most of their pre-brecciation texture and mineralogy: clots of pyrophyllite with remnants of white micas rimmed by sulfides and clusters of rutile or anatase are set in a silicified groundmass with early quartz veinlets (mostly B-type). In the monolithic breccia (drill hole AR-82 at 460, 550, 595, and 620 m depth, Fig. 3; drill hole AR-80, between 4 and 166 m depth; Fig. 7), clasts of the metasedimentary rock contain pyrophyllite replacing white micas of the pervasive phyllic alteration (Fig. 8). The heterolithic breccia contains zones with intense silicified clasts (Fig. 3) and in the upper levels the clasts consist mainly of residual quartz crystal aggregates with typical vuggy texture (Fig. 4); they contain numerous trails of vapor-rich fluid inclusions.

6.5.2. Brecciation stage

At the scale of the deposit, hydrothermal breccias are elongated subparallel to Quebrada Minas (Fig. 1) with downwards converging contacts of between 45 and 90°. At lower levels the contacts commonly become shallower resulting in a flat-bottomed shape (BHP, 1999). In the analyzed section, the hydrothermal breccia bodies located at the center of the section and to the east, in the Trampeadero porphyry and the metasedimentary rock, have four distinct facies. The different facies have the following characteristics:

6.5.2.1. Heterolithic breccia. It is a hydrothermal breccia that was intersected by drill hole AR-82 up to 300 m below the surface (Figs. 2b and 3). It consists of subangular to subrounded, poorly sorted (0.3 cm to large clasts of 40–50 cm in diameter) fragments set in a matrix that varies from clastic to hydrothermal cement and contains vugs (between 0.2 mm to 2 cm diameter) (Fig. 4). It also has several large (10 m) clasts of strongly altered and silicified porphyry and metasedimentary rock (Fig. 3). In the upper levels, the clasts consist mainly of quartz aggregate and the following types have been identified: (1) porphyry clasts, with quartz phenocryts (phenoclasts?) surrounded by very fine-grained quartz aggregates of the silicified groundmass; (2) clasts of metaquartzite, constituting fine polycrystalline quartz aggregates with relic schistosity, and (3) clasts of different generations of quartz veins and veinlets. Less frequent are clasts of polygranular pyrite (with subordinated covellite) aggregates. The clastic matrix is dominated by sand- to silt-sized, subrounded to subangular quartz and altered and mineralized rock fragments. The breccia varies from matrix-supported (40–50% matrix) to clast-supported (10–15% matrix) and in the first case the fragments are more rounded and show evidence of strong physical and chemical abrasion (Fig. 4). Between 10 and 196 m depth, the breccia is mainly

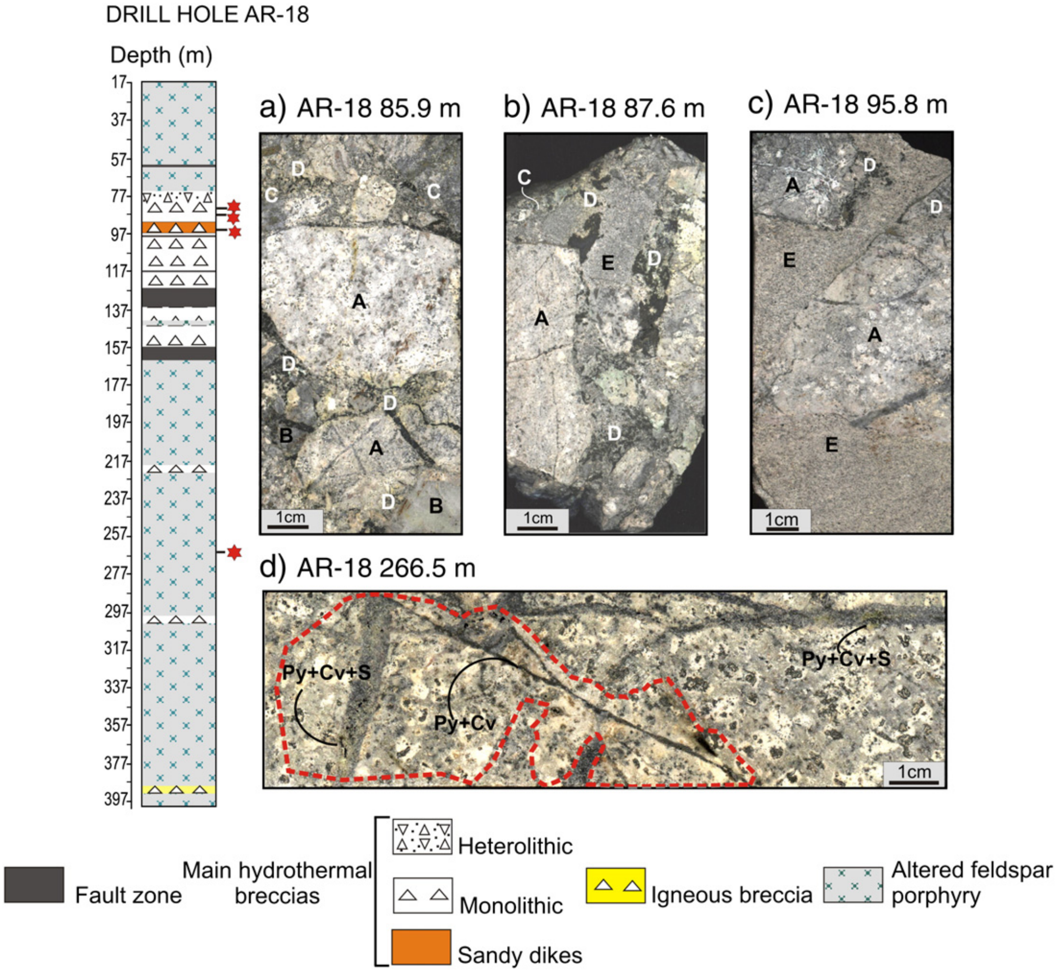

Fig. 6. Photographs illustrating monolithic breccia, sandy dike, and assemblages of the advanced argillic alteration–mineralization stage cut by drill hole AR-18. a): Clast-supported monolithic hydrothermal breccia with fragments of altered Trampeadero porphyry A and quartz veinlets B set in a matrix C of similar composition and cemented by sulfides (visible covellite) and alunite D that invade the clasts. b): Similar breccia also contains clasts of a sandy dike E. c): A sandy dike E cuts the hydrothermal breccia. d): Trampeadero porphyry with pyrophyllite, disapore, and kaolinite in clots, native sulfur in voids, and pyrite + covellite ± diaspore ± alunite + native sulfur veinlets and clots overprinting the phyllic alteration, B-type quartz veinlets and andalusite (most affected zone shown in the photo).

matrix-supported, and the clastic matrix is composed by subangular, subrounded fine-grained quartz and altered rock fragments with hydrothermal cement. At approximately 260 m depth, after a zone of intense faulting, the breccia becomes mainly clast supported (Figs. 3 and 4).

6.5.2.2. Monolithic breccias. They occur in drill hole AR-18, between 77 and 157 m, at 220, and at 300 m depth (Fig. 5) and intersects a clast-supported hydrothermal breccia with angular to subrounded fragments of the Trampeadero feldspar porphyry and its early quartz veinlets set in a clastic matrix replaced by hydrothermal cement with minor porosity (0.1–0.5 mm diameter spaces) (Fig. 6). Unlike the heterolithic breccia, clasts in this breccia have preserved most of their pre-brecciation texture and mineralogy. Similar breccia affects the altered metasedimentary rock below the heterolithic breccia (drill hole AR-82 at 460, 550, 595, and 620 m depth; Fig. 3) and farther east (drill hole AR-80, between 4 and 166 m depth; Fig. 7), and consists of altered angular metasedimentary rock fragments that range in size from pebble to cobble (some are boulder) in a matrix composed of hydrothermal cement with minor clastic rock flour component (5%). Locally, minerals in the cement are poorly annealed and have open void spaces (Fig. 8). Both types of monolithic breccias (with Trampeadero porphyry and metasedimentary rock fragments) vary from typical jigsaw type to weakly rotated (Figs. 6 and 8). Intensely fractured and altered feldspar porphyry resembling a jigsaw (Sillitoe, 1985) or shatter (Baker et al., 1986) breccia without significant fragment displacement occurs at AR-82 below the heterolithic breccia, between 320 and 390 m depth, in transition to unbrecciated deeper zones (Fig. 3).

6.5.2.3. Sand and pebble breccia dikes. Drill hole AR-82 intersects several matrix-supported sand to pebble breccia dikes that intrude the heterolithic breccia and the altered metasedimentary rock (Fig. 3). At AR-18 95.8 m depth, a sandy breccia dike cuts the monolithic Trampeadero porphyry breccia, but at higher levels; fragments of similar breccia dikes with fragments of the Trampeadero breccia are cemented by hydrothermal minerals, indicating more than one brecciation stage (Figs. 5 and 6). The analyzed breccia dikes consists of very fine-grained matrix composed of rounded quartz and quartz aggregates of 0.1 to 0.5 mm in diameter with interstitial hydrothermal minerals.

6.5.3. Post-brecciation stages

In the Seca Norte jigsaw breccia (AR-82, between 320 and 390 m depth; Fig. 3), the open space between clasts, the fractures within clasts, and early reopened quartz veins are filled with alunite + diaspore + native sulfur (Fig. 4). Sectors of the Trampeadero porphyry cut by AR 18 (between 17 and 77 m depth and at 266 m depth, Fig. 5), contain diaspore ± alunite + native sulfur veinlets and clots and native sulfur in voids.

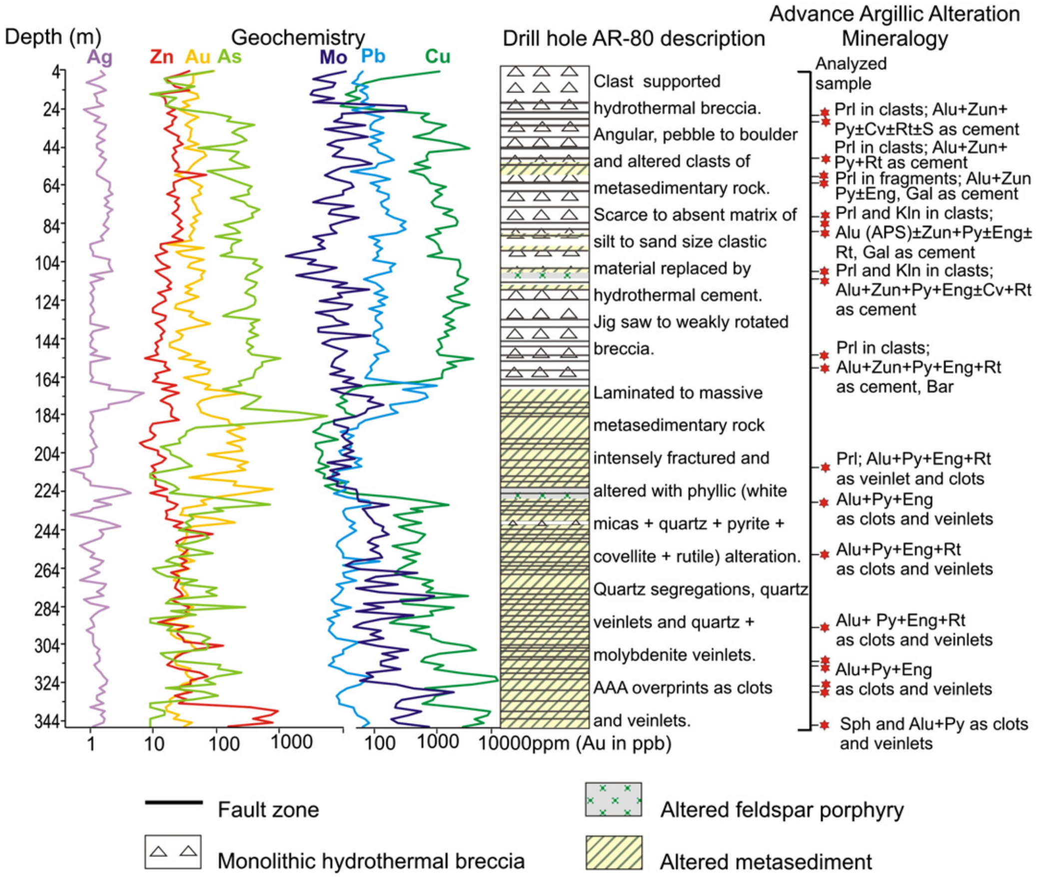

Fig. 7. Geochemistry, geology, alteration types, and mineralogy of the advanced argillic alteration cut by drill hole AR-80 in the N 6969400 section. Data based on BHP (1999) and this contribution. See explanation of symbols in Fig. 3.

In the heterolithic hydrothermal breccias, alunite and aluminophosphate-sulfates (APS) ± diaspore ± zunyite ± native sulfur ± rutile or anatase replaces the matrix, cements the clasts, fills open spaces between fragments, microfractures and stringers that cut fragments and the numerous voids within fragments (Figs. 3 and 4). Where breccia clasts are dominated by the altered metasedimentary rock, zunyite is more abundant than diaspore. Alunite (APS) + diaspore replaces the matrix in the Trampeadero monolithic breccia, fills veins and veinlets that cut fragments, and sometimes invades early pyrophyllite-rich clots and quartz veins, whereas native sulfur most commonly fills voids (Figs. 5 and 6). In the monolithic breccia with metasedimentary rock fragments, the cement consists of diaspore ± zunyite in AR-82 (Fig. 3), and alunite (and APS) + zunyite + rutile or anatase ± native sulfur, barite in AR-80 (Figs. 7 and 8) that also invades the fragments through fractures and stringers (Fig. 8). The sand to pebble breccia dikes contains interstitial alunite ± rutile or anatase.

Late alunite and kaolinite veinlets or clots cut and overprint early assemblages in the breccias and in unbrecciated sectors intersected by drill holes AR-82 (Fig. 3) and AR-18 (Fig. 5). Kaolinite also fills interstices between white micas of the phyllic halo intersected by drill hole AR-9.

7. Mineralization in the E–W section along 6969400m

Mineralization is the result of three sequential main stages consisting of porphyry, epithermal, and supergene enrichment. Sulfide assemblages and their textures were useful to identify each stage and their paragenesis. The porphyry Cu–Mo–Au mineralization, represented by two main sulfide assemblages, occur mainly as fine-grained disseminations, also in B-type quartz veinlets, and stringers in the phyllic envelope below the hydrothermal breccias. Clasts containing porphyry stage veinlets and mineralization are also common within the hydrothermal breccias. Epithermal Cu–As–Zn–Pb–Au–Ag (Sn) sulfides are coarser grained, spatially zoned, and deposited as cement within the hydrothermal breccias during several mineralization events; at deeper level, they fill veinlets that cut the phyllic alteration in the unbrecciated Trampeadero porphyry and metasedimentary rocks.

7.1. Porphyry stage

Pyrite + chalcopyrite ± molybdenite ± bornite occur in the Seca Norte porphyry with relic potassic patches and phyllic alteration. Sulfides occur as subhedral (pyrite, molybdenite) to anhedral (chalcopyrite and bornite) fine grains (0.5 mm average) disseminated within phyllosilicate clots, rimming hydrothermal K-feldspar, and filling hairline fractures that crosscut the phyllic alteration assemblage and early barren quartz veinlets. Copper grade varies between 0.11 and 0.60% Cu in the hypogene sulfide zone (Fig. 11). Molybdenum grades are low (average = 196 ppm; Fig. 11). The dominant sulfide association with the phyllic alteration replacing the metasedimentary rock and in the Trampeadero porphyry is pyrite ± covellite ± molybdenite. They occur as fine-grained disseminations accompanying phyllosilicates, delineating phyllosilicate clots or in veinlets with quartz. Pyrite in subhedral to euhedral fine grains (0.04 to 0.15 mm) is always volumetrically more abundant than anhedral hypogene covellite (<0.01 mm) and tabular molybdenite crystals; it contains microinclusions of pyrrhotite, chalcopyrite, and bornite. Chalcopyrite and bornite grains are present in samples AR-82 552, 624 and 655 m,

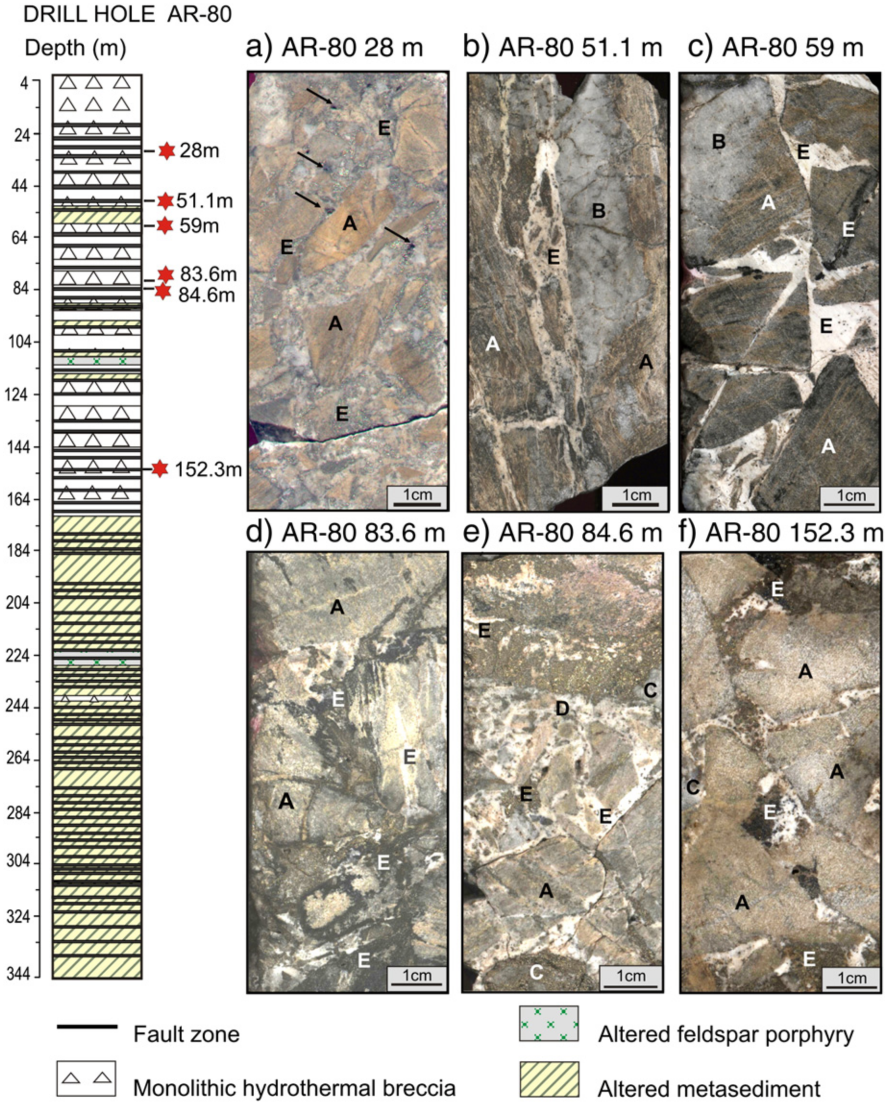

Fig. 8. Photographs illustrating monolithic breccia types and hydrothermal infill of the advanced argillic alteration–mineralization stage cut by drill hole AR-80. Examples of clast-supported monolithic, weakly rotated (a to e) to jig-saw (f) hydrothermal breccia. Altered metasedimentary rock clasts A with metamorphic B and hydrothermal C quartz veinlets and minor rock flour D are cemented by alunite + pyrite + zunyite + enargite (covellite ± barite, galena) E that also invades the clasts. See open space texture in a) (arrow).

AR-18 387 and 393 m, and in AR-80 and relict chalcopyrite and bornite cores have been observed in covellite (samples AR-82 552, 655 m, AR-18 249 and 393 m). Copper grades vary between 0.001 and ~0.5% in the altered metasedimentary rock and between 0.012 and 0.32% in the altered Trampeadero porphyry (Figs. 3, 5, 7, and 11); higher Cu grades (0.5 to 0.9%; Figs. 3, 5, 7, and 11) correspond to samples with superposed veinlets of the high-sulfidation epithermal stage. The altered metasedimentary rock in the center of the section contains several zones with the highest Mo grades (>1000 ppm; Figs. 3 and 11) of the entire phyllic envelope, and here molybdenite occurs as centerlines and at the margins of the B-type quartz veinlets and as thin and discontinuous fracture fillings in equilibrium with white mica. Other similar veinlets with high Mo grades are also present locally in the altered Trampeadero porphyry (Figs. 5 and 9) and east, in the metasedimentary rock (Fig. 7). Some quartz veinlets have been reopened and filled with late sulfide assemblages (e.g., samples AR-82 356 and 359 m) (Fig. 9), others appear without sulfides (Fig. 9).

7.2. Epithermal stage

In the brecciated and altered Seca Norte feldspar porphyry (AR-82, between 320 and 390 m depth, Fig. 3), the open space between clasts, the fractures within clasts, and early reopened quartz veins are filled with pyrite + covellite + enargite ± molybdenite ± kuramite and arsenopyrite with the AAA assemblage (Fig. 4). Pyrite crystals are rimmed by arsenopyrite and a second pyrite generation. Molybdenite is in clusters of crystals and along hairline fractures; it could have been remobilized from early phyllic alteration. This brecciated porphyry has locally high Cu (>1 to 2.4% Cu), As (0.15%), Zn (0.15 and 0.3%), and Pb (0.13%) grades (Figs. 3 and 11).

In the clast-supported heterolithic hydrothermal breccia (AR-82 between 260 and 320 m depth), covellite + pyrite ± enargite ± molybdenite ± kuramite, and arsenopyrite accompanies AAA assemblages as hydrothermal cement (Figs. 3 and 4). In contrast to the sulfides of the phyllic halo, pyrite and covellite are coarse grained. Covellite occurs as euhedral, hexagonal sheets or prismatic crystals that locally reach up to 1 cm in diameter (Fig. 4) and is hypogene in origin; it contains numerous vermicular micro-inclusions of pyrite. Pyrite crystals are rimmed by a second anhedral and porous pyrite generation or by arsenopyrite; another breccia sample (AR-82 259 m) contains pyrite as small and very porous crystals (melnikovite) and as large and euhedral crystals that enclose molybdenite, probably indicating it has been remobilized. Late veinlets of pyrite (with alunite; AR-82 265 m) cut the breccia (Figs. 3 and 4). This breccia zone

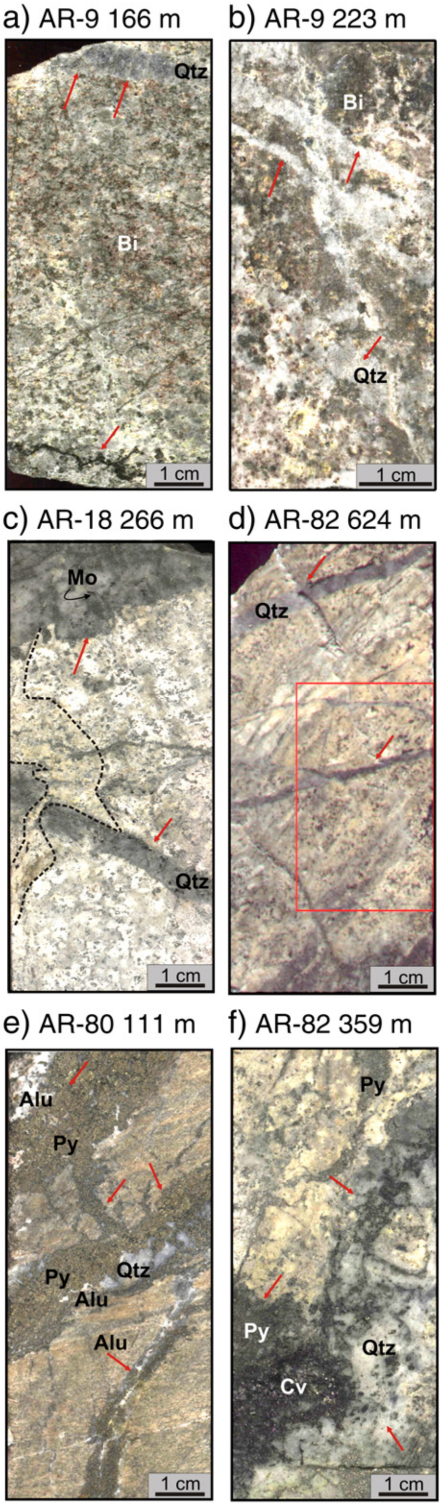

Fig. 9. Photographs illustrating alteration and mineralization textures at the Agua Rica porphyry Cu stage. a) and b) show remnants of potassic alteration and pyrite + chalcopyrite ± molybdenite mineralization in the Seca Norte porphyry. The hydrothermal biotite occurs as very fine brownish–greenish plates in aggregates. See irregular biotite + sulfides stringers and a B-type quartz veinlet in a) and A-type quartz veinlets in b). c) and d) show examples of different phyllic alteration textures in the Trampeadero porphyry and in the metasedimentary rock, respectively, with B-type veinlets and molybdenite at the margin of the veinlet (c); other veinlets appear without sulfides (d). A patch of advanced argillic alteration overprints the altered porphyry (c). e) and f) show metasedimentary rock and porphyry with phyllic alteration, respectively, and reopened, B-type quartz veinlets filled with late pyrite, covellite, and alunite. Alu = alunite; Bi = biotite; Mo = molybdenite; Py = pyrite; and Qtz = quartz.

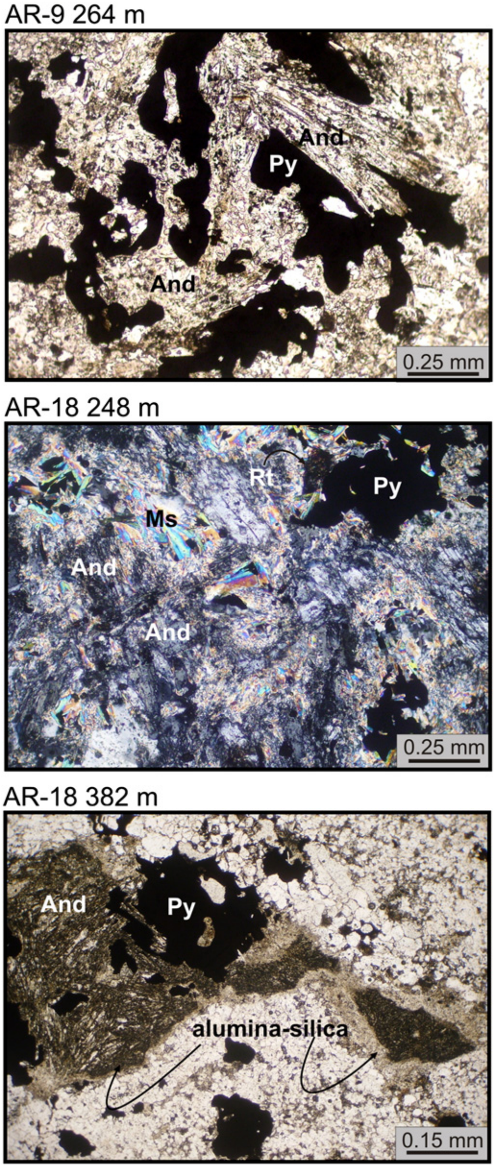

Fig. 10. Photomicrographs illustrating the transitional alteration in the Seca Norte and Trampeadero porphyries: clots of andalusite ± sulfides ± quartz rimmed and partially replaced by white mica that also has grown within a submicroscopic and cloudy alumina–silica material, which fringes corroded andalusite crystals. And = andalusite; Ms = white micas; Py = pyrite; and Rt = rutile or anatase.

contains the highest grades of hypogene copper (1%, 2.7%, and 3.7% Cu at 264–270 m, 284–292 m, and 302–304 m depth, respectively) and arsenic (between 0.1 and 0.27% As at 234–270 m depth) (Figs. 3 and 11).

In the matrix-supported heterolithic breccia, between 10 and 196 m depth, mineralization consists of pyrite, sphalerite, emplectite, and aikinite. Pyrite contains inclusions of chalcopyrite, pyrrhotite, bornite, and rutile or anatase. Pyrite grains are corroded and rimmed by at least two generations of porous and anhedral pyrite (melnikovite; AR-82 146, 151, 152, and 163 m) (Figs. 3 and 4). Emplectite and sphalerite (AR-82 160 m) rim pyrite and aikinite fills voids. At AR-82 85 m depth, abundant pyrite cements fragments of hydrothermal breccia clasts (Fig. 3) and is clear evidence of more than one episode of brecciation. Veinlets of sphalerite (AR-82 96 m), banded pyrite + sphalerite (AR-82 122.90 m), and fine-grained pyrite (AR-82 146 m, 166 m) cut the breccia (Figs. 3 and 4). The last veinlet type has a halo

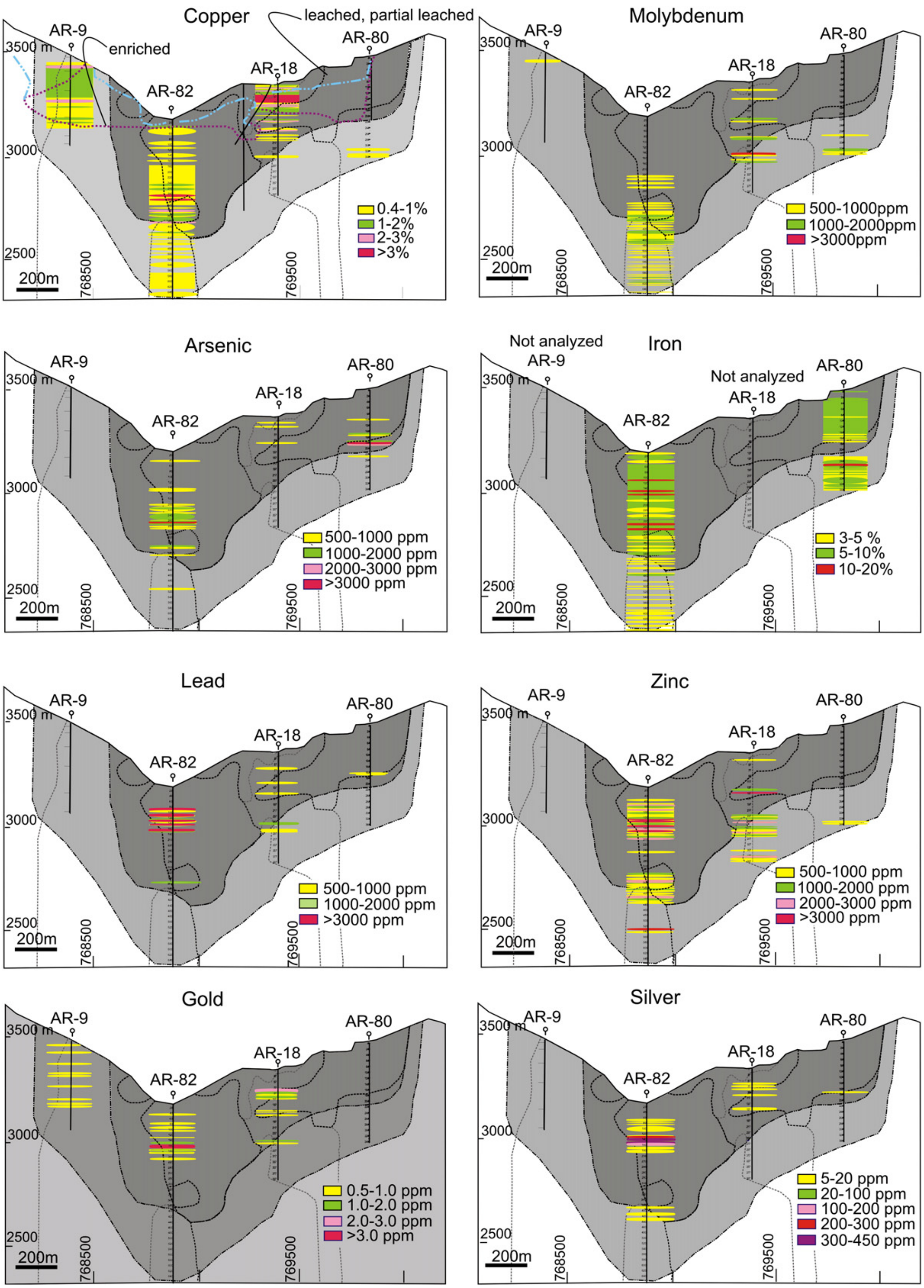

Fig. 11. Geochemistry of the section illustrating copper, molybdenum, arsenic, iron, lead, zinc, gold, and silver grade patterns. Grades data come from BHP (1999).

of platy alunite crystals with pseudocubic core of alumino-phosphates-sulfates (APS). Copper and arsenic grades are generally lower than 1%, with most common values between 0.2 and 0.6% Cu, and 0.001 to 0.03% As with locally 0.08% As (Figs. 3 and 11). In contrast to Cu and As grades, this breccia is enriched in Zn (0.1–0.55%) and Pb (0.1–0.53%) (Figs. 3 and 11). High Au and Ag grades (1–1.8 g/t Au and 239–325 g/t Ag at 146–154 m depth, and 1.7–5.6 g/t Au at 160–164 m depth; Figs. 3 and 11) display a positive correlation with Pb and Zn in drill hole intersections in which gold grades accompany emplectite, aikinite, and sphalerite. Native gold (electrum) has been observed as up to 2 μm grains in cracks and microfractures in quartz.

The monolithic hydrothermal breccias are cemented by pyrite + covellite (AR-82 at 460, 550, 595, and 620 m depth; Fig. 3. AR-18, between 77 and 157 m, at 220, and at 300 m depth; Fig. 5) and pyrite + enargite, galena and traces of covellite farther east (AR-80, between 4 and 166 m depth; Figs. 7 and 8) in both cases accompanying the advanced argillic mineral assemblage. Covellite occurs as subhedral to euhedral crystals up to 1 mm long. Hypogene Cu grades notably decreases eastwards (>1% Cu, with sectors up to 3.4% Cu in the brecciated Trampeadero porphyry towards <0.35% Cu in the brecciated metasedimentary rock) as does Zn, Au, and Pb, whereas As contents are higher in the brecciated metasedimentary rock (Figs. 3, 5, 7, and 11). The matrix-supported sand to pebble breccia dikes contain interstitial pyrite ± covellite.

7.3. Supergene overprint

Supergene leaching and secondary enrichment have been more pronounced on the west side of the section, affecting more than 350 m of the altered and mineralized Seca Norte feldspar porphyry (Fig. 2b). Limonites with traces of pyrite and smectite are present in the first 50 m of the leached cap. Downwards, in the enrichment blanket, chalcopyrite crystals are rimmed by covellite ± digenite (Table 1) or cut by numerous fractures filled with covellite. This sector with a supergene overprint has high Cu grades (up to 2.1% Cu; Fig. 11) and also contains moderate gold grades (sectors with 0.5 to 0.8 g/t Au; Fig. 11). Eastwards, at shallow depths (up to 98 m depth), digenite replaces covellite in the cement and veinlets of the hydrothermal breccia, as well as in the Trampeadero porphyry (Fig. 2b).

8. Mineral distribution and composition

The distribution of the most important minerals of each alteration and mineralization stage is illustrated in Figs. 12 and 13. Fig. 14 shows examples of their microscopic arrangement and textures.

Table 2 summarizes the chemical composition of biotite and white micas from the potassic patches and from the phyllic alteration, respectively. In this study the structural formula of micas were recalculated on the basis of $O_{20}(OH)_4$ anion content (Newman and Brown, 1987). Representative biotite crystals (n = 11) have the compositional range $K_{1.78-1.67}Na_{0.05-0.02}(Al_{0.42-0.00}Mg_{3.77-3.22}(Si_{5.42-4.82}Al_{3.18-2.58})O_{10}(OHF_{1.88-1.40})_4$. K is the dominant cation in the interlayer with only traces of Ca, Na, Sr, and Ba. In the octahedral site, the most abundant divalent cation is Mg with minor Fe^{2+}, and traces of Al, Ti, and Mn^{2+}. Biotite grains have Mg/(Mg + Fe) (XMg) values between 0.69 and 0.78 and locally very high F content (>4% F). Such a high XMg incorporates more F, a crystal–chemical effect referred to as the Fe–F avoidance principle (Munoz, 1984). Biotite composition is similar to relic biotites in the phyllic halo of other porphyry Cu deposits (see Selby and Nesbitt, 2000). White micas + illite occur in the transitional alteration and in most of the phyllic envelope, only white mica in a sector of the metasedimentary rock with phyllic alteration cut by drill hole AR-80, and only illite in the advance argillic alteration zone, in breccias clasts and matrix with pyrophyllite. The analytical results from 37 microprobe analyses for white micas are $K_{1.91-1.08}Na_{0.09-0.0}(Al_{3.97-3.60}Mg_{0.37-0.09}Fe_{0.26-0.01}Ti_{0.07-0.0})(Si_{6.53-6.05}Al_{1.95-1.47})O_{10}(OHF_{0.54-0.0}Cl_{0.02-0})_4$. Based on these results, all analyzed micas have less K and Na and more Si than ideal muscovite. Thus, with few exceptions that have total interlayer charge as high as 1.5 and corresponds to I/S (AR-9 264 m), they are illitic white mica in composition and similar to white micas of the phyllic alteration in other porphyry copper deposits (Perry et al., 2002). Illite was identified by XRD in the <2 μm fraction of the 53 analyzed samples. Illite is not expandable and was distinguished in air-dried, ethylene glycol-saturated, and calcinated samples by the sharp reflection of the 001 peak at 10 Å, and by the successive reflections of 2nd, 3rd, and 4th order peaks. Based on the illite intensity ratio (Ir), with values between 0.92 and 1, no expandable interlayers were found, except for illite from sample AR-9 264 m, with an Ir > 1 and could contain minor expanding component (<10%). Determined illite polytype in the <2 μm fraction of 12 samples corresponds to *2M₁*.

Table 3 summarizes the chemical composition of andalusite (n = 6 analyses), pyrophyllite (n = 62), diaspore (n = 4), zunyite (n = 15), alunite (n = 25), svanvergite (n = 6), and woodhouseite (n = 4). Andalusite occurs in deeper zones of the Seca Norte and Trampeadero porphyries with phyllic alteration, and is not related to other advanced argillic alteration minerals (Fig. 12). It was identified petrographically, by X-ray diffraction, and its overall chemical composition (Table 3). Pyrophyllite is widespread in the advanced argillic alteration zone and occurs with diaspore and zunyite up to 480 m depth in the centrally located heterolithic and monolithic jigsaw breccias (Fig. 12). Pyrophyllite occurs with diaspore up to 270 m in the Trampeadero monolithic breccia and further east, with zunyite up to 160 m depth and with alunite up to 214 m in the brecciated metasedimentary rock (Fig. 12). However, in all cases pyrophyllite predates the formation of diaspore, zunyite, and alunite (Fig. 14: AR-82 146 m; AR-80 86.7 m). Pyrophyllite was distinguished by its X-ray diffractometry peaks at 9.20, 4.42, and 3.07 Å, respectively, in air-dried samples, after ethylene glycol saturation, and in calcinated samples. Table 3 summarizes the chemical compositions of pyrophyllite and the structural formula was recalculated on the basis of $O_{20}(OH)_4$ anion content (Newman and Brown, 1987). The analytical results from 62 microprobe analyses of representative crystals are $K_{0.17-0.0}(Al_{4.1-3.93}Fe_{0.06-0.0})(Si_{8.0-7.51}Al_{0.49-0.0})O_{10}(OHF_{0.16-0.04}Cl_{0.08-0.0})_4$. Like the range of natural compositions, the Si/R^3 ratios, ranging from 1.88 to 2, slightly deviate from the ideal ratio of 2. The Al atoms are lower than 0.49 in the tetrahedral site, which represents only 6% of the tetrahedral cations, and makes up about 99% of the octahedral cations. Most analyses have total interlayer cations less than 0.1 and fluorine in a range from 0.16 to 0.04 replacing the OH site and this replacement is higher in pyrophyllite samples from the heterolithic and the Trampeadero monolithic breccias. Zunyite and diaspore were identified by microscopy, X-ray methods, and microprobe analysis (Table 3). Zunyite crystals from the heterolithic (AR-82) and monolithic (AR-80) breccias show lower to similar chlorine (2.2 to 3.1%) and much higher fluorine (3.7 to 8.5%) contents than normal zunyite composition (3.06% Cl and 3.28% F; Deer et al., 1966).

Alunite is widespread and extends beyond the limit of the main advanced argillic zone, as veinlets and clots cutting the phyllic alteration. Alunite occurs as fine crystals (0.02 mm) and felted aggregates, in well terminated rhombohedral crystals up to 1 mm long with facets that lined open spaces in the breccias, typically plumose and platy with parallel and radial extinctions, probably reflecting various generations of alunite. It is in contact with diaspore, zunyite, pyrite, covellite, and enargite, filling veinlets, coatings on breccia fragments or sulfides veinlets or in clots surrounded by pyrophyllite after illite. Aluminum-phosphate-sulfate (APS) minerals of hypogene origin have been found as microinclusions within or next to alunite. For example, euhedral, trapezoedric and pseudocubic, zoned APS inclusions, ~30 to 102 μm in diameter, occur surrounded by alunite (Fig. 14, AR-18 266 m). The quantitative identification of each zone record Sr–Ba–S-bearing trapezoedric cores, Ca–P–S-rich cubic section and K–S rim (Fig. 14). In other cases, APS inclusions consist of microlaminar aggregates (Fig. 14: AR-18 85 m; AR-80 86.7 m) or euhedral trapezoedric crystals. Such inclusions are common in high sulfidation epithermal systems, and similar occurrences have been documented from the Nansatsu district, Japan (Hedenquist et al., 1994), Summitville, Colorado (Stoffregen and Alpers, 1987), and Rodalquilar, Spain (Arribas et al., 1995). Considering the general chemical formula $RAl_3(PO_4)_{1+x}(SO_4)_{1-x}(OH)_{6-x}(H_2O)_x$, alunite chemical compositions are somewhat variable and

Table 1

Representative chemical compositions of sulfides from the potassic and phyllic alteration zones.

Sulfide alteration sample N° (wt.%)	Pyrite			Pyrite			Chalcopyrite			Chalcopyrite		
	Potassic			Phyllic			Potassic			Phyllic		
	AR9-166 m	AR9-166 m	AR9-264 m	AR9-90 m	AR82-552 m	AR9-264 m	AR9-166 m	AR9-264 m	AR9-264 m	AR82-552 m	AR18-249 m	AR18-249 m
S	53.42	52.47	52.92	52.47	54.31	54.20	35.01	34.71	34.48	34.47	34.84	34.72
V	0.00	0.25	0.00	0.00	0.00	0.00	0.00	0.00	0.00	0.00	0.00	0.00
Fe	46.39	45.87	46.29	45.77	46.10	46.80	30.32	30.67	30.45	28.53	28.46	28.45
Cu	0.07	0.20	0.00	0.19	0.05	0.00	34.09	33.61	34.12	36.13	35.94	36.55
Zn	0.74	1.10	0.46	0.83	0.00	0.00	0.73	0.72	0.50	0.00	0.00	0.00
As	0.07	0.20	0.07	0.11	0.00	0.00	0.08	0.00	0.00	0.00	0.00	0.00
Ag	0.00	0.00	0.00	0.00	0.00	0.00	0.00	0.00	0.00	0.00	0.00	0.00
Sn	0.16	0.11	0.06	0.28	0.00	0.00	0.00	0.18	0.13	0.00	0.00	0.00
Sb	0.08	0.00	0.20	0.24	0.00	0.00	0.00	0.11	0.00	0.00	0.00	0.00
Au	0.00	0.00	0.00	0.00	0.00	0.00	0.00	0.00	0.00	0.00	0.05	0.00
Pb	0.00	0.00	0.00	0.00	0.00	0.00	0.00	0.00	0.00	0.00	0.00	0.00
Total	100.93	100.20	100.00	99.89	100.46	101.00	100.23	100.00	99.68	99.18	99.29	99.72

Sulfide alteration sample N° (wt.%)	Bornite			Covellite			Covellite			Digenite		
	Phyllic			Potassic			Phyllic			Potassic		
	AR82-552 m	AR82-552 m	AR82-552 m	AR9-166 m	AR9-166 m	AR9-166 m	AR82-552 m	AR82-552 m	AR18-249 m	AR9-187 m	AR9-187 m	AR9-166 m
S	34.78	34.50	34.19	31.59	32.64	32.64	33.92	33.92	30.12	22.92	23.61	24.93
V	0.07	0.00	0.00	0.00	0.00	0.00	0.00	0.00	0.00	0.00	0.00	0.00
Fe	20.29	19.33	18.77	0.66	0.45	0.17	0.18	0.69	2.49	0.00	0.00	0.49
Cu	44.03	45.57	46.94	67.61	67.00	67.20	64.88	64.90	66.56	77.06	75.95	74.32
Zn	0.27	0.00	0.00	0.10	0.20	0.00	0.00	0.00	0.00	0.00	0.00	0.06
As	0.00	0.00	0.00	0.00	0.00	0.00	0.00	0.00	0.00	0.00	0.00	0.00
Ag	0.00	0.05	0.05	0.00	0.00	0.00	0.05	0.00	0.06	0.00	0.00	0.00
Sn	0.31	0.00	0.00	0.00	0.00	0.00	0.00	0.00	0.00	0.00	0.00	0.00
Sb	0.25	0.00	0.00	0.00	0.00	0.00	0.00	0.00	0.00	0.00	0.00	0.00
Au	0.00	0.00	0.00	0.00	0.00	0.00	0.00	0.08	0.07	0.00	0.00	0.00
Pb	0.00	0.00	0.00	0.00	0.00	0.00	0.00	0.00	0.00	0.00	0.00	0.00
Total	100.00	99.45	99.95	99.96	100.29	100.01	99.04	99.59	99.29	99.98	99.56	99.80

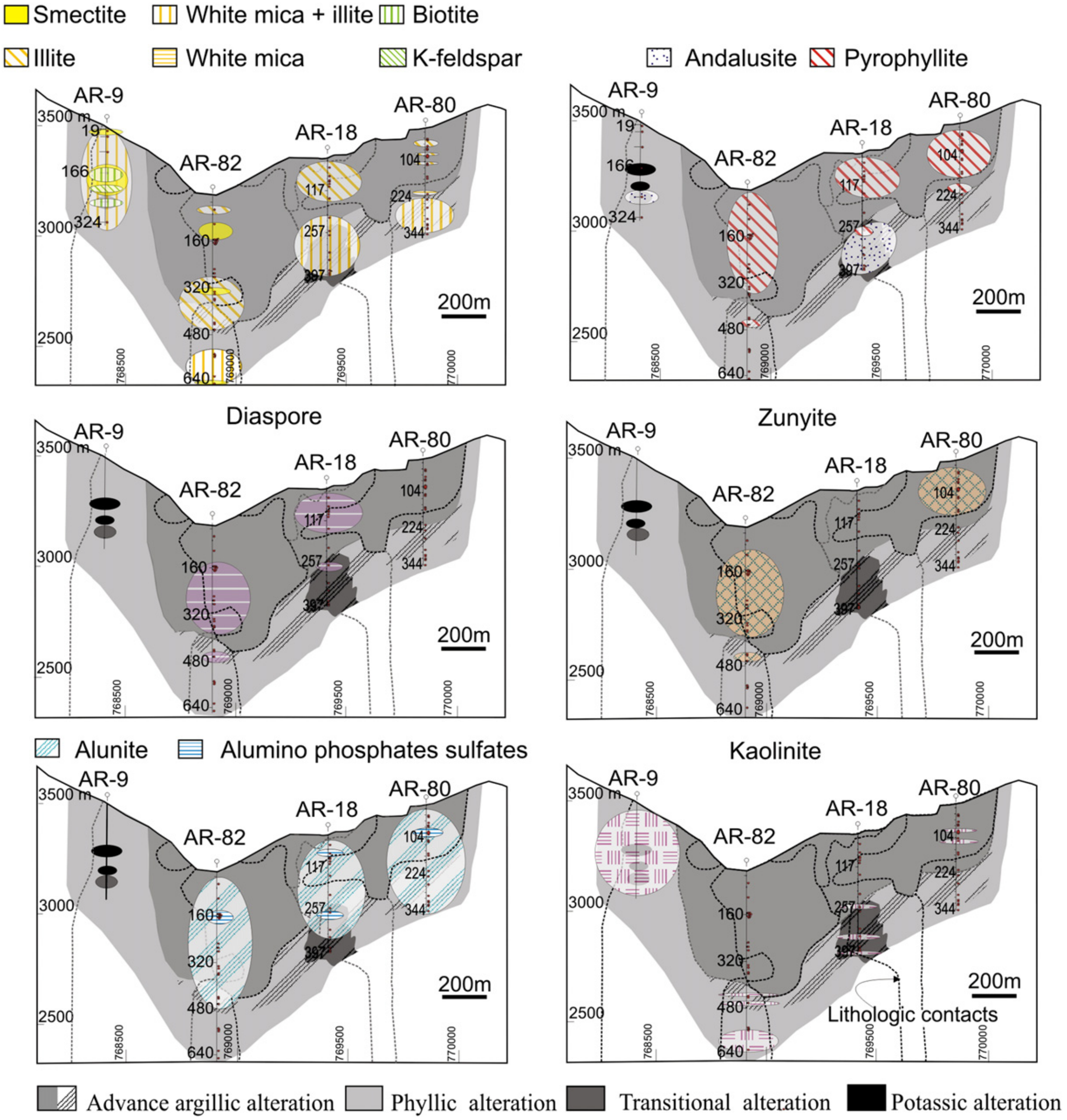

Fig. 12. Distribution of biotite, K-feldspar, and phyllosilicates of the potassic and phyllic alterations and pyrophyllite, diaspore, zunyite, alunite, alumino phosphate-sulfates and kaolinite of the advanced argillic alteration, including andalusite, along the E-O6969400 N cross section.

some crystals show molar amounts of PO_4^{3-}, Sr^{2+}, and Ca^{2+} (Table 3), and could indicate some solid solution between alunite and APS or they may reflect the presence of APS grains within the analyzed crystal. In other samples, the molar amount of PO_4^{3-} exceeds the molar $Sr^{2+}+Ca^{2+}$ content, suggesting the presence of other cations or some hydroxyl group in the formula. Finally, some crystals are enriched in Sr^{2+}. The chemical composition of the analyzed APS minerals corresponds to solid solutions between woodhouseite and svanbergite (Table 3), the Ca and Sr end-members for which $x=0$, and members of the crandallite–goyazite series, for which $x=1$.

Kaolinite has been identified in the phyllic halo as a late mineral in clots (AR-9, AR-18) or in veinlets (AR-82 440 and 460 m) and in the Trampeadero (AR-18 147 m) and the metasedimentary rock (AR-80 83.6 and 113 m) monolithic breccias. It was distinguished by XRD in oriented aggregates by the sharp reflection of the (001) peak at 7.16 Å, and for the (002) peak at 3.56 Å, which disappear when calcinated at 550 °C.

Table 1 summarized the chemical compositions ($n=83$) of hypogene and supergene sulfides from the porphyry stage and Fig. 13 shows their distribution. Pyrite is widespread in the entire section, followed by covellite, chalcopyrite, and bornite and in all cases they are fine-grained which makes easy their recognition when two mineralization stages are superposed in the same sample (i.e., in breccias). Molybdenite from the porphyry and the epithermal stages has not been differentiated in the figure. The chemical compositions of pyrite and chalcopyrite show variable concentration of different trace elements. Among these, Zn is the most abundant trace element (up to 1.10 wt.%), followed by Sn, Sb, and As. Table 4 summarizes the chemical compositions ($n=133$) of main sulfides from the epithermal stage. Coarse-grained pyrite typical of the advanced argillic alteration stage is widespread (Fig. 13); like alunite, it extends beyond the limit of the main advanced argillic zone as veinlets cutting the phyllic alteration (Fig. 9, AR-80 111 m.). Pyrite crystals are zoned and at least three generations of pyrite have been identified in samples

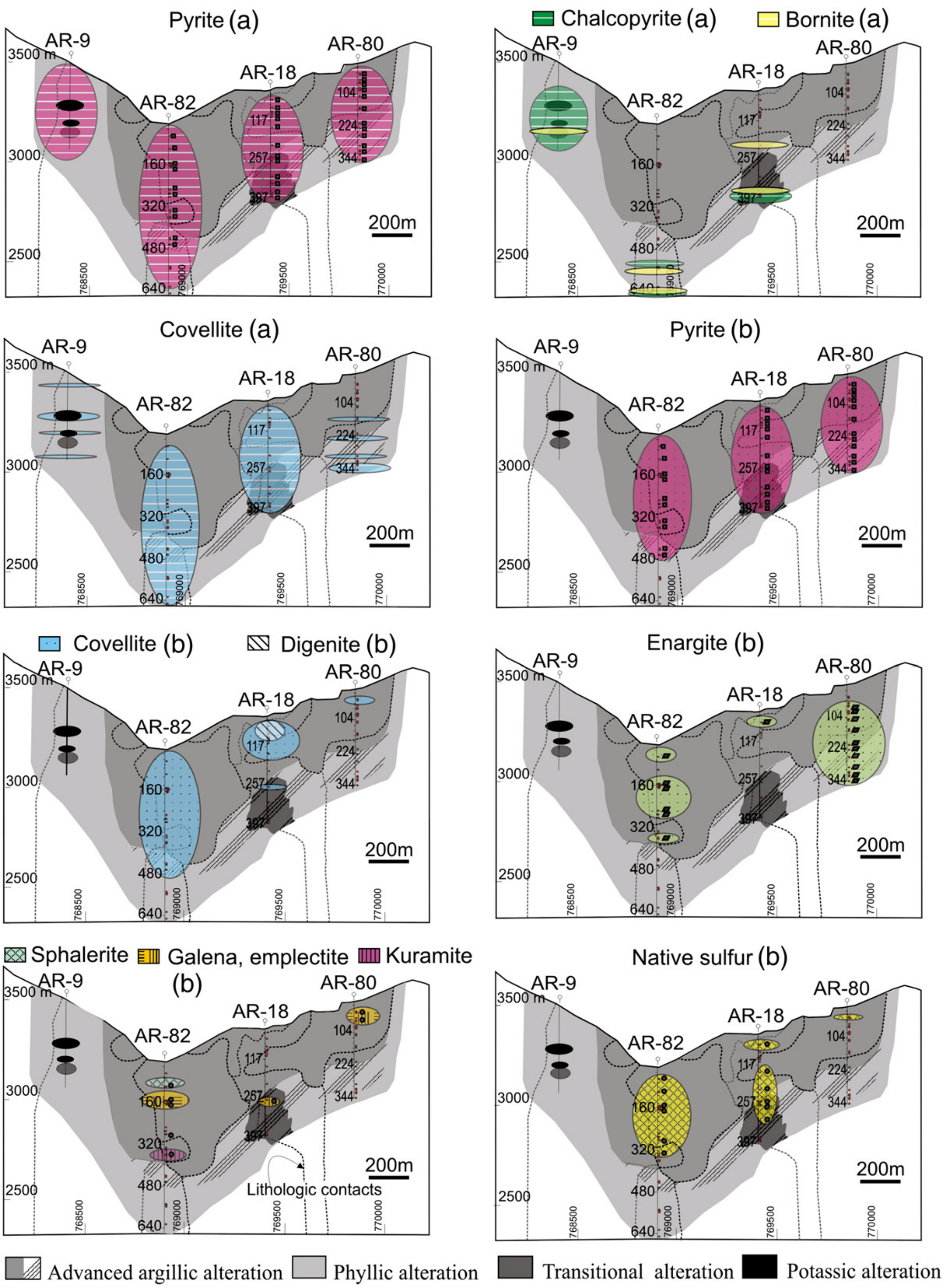

Fig. 13. Distribution of pyrite, chalcopyrite, bornite, covellite (digenite), enargite, native sulfur, and other sulfides of the porphyry (a), advanced argillic and supergene (b) mineralization stages along the E-O6969400 N cross section.

from the hydrothermal heterolithic breccia. Pyrite rims are slightly enriched in Zn and Cu relative to the cores, also in As, Sb, and Ag. Coarse-grained covellite is abundant along the central heterolithic, jigsaw breccias, below, in the brecciated metasedimentary rock, and in the Trampeadero breccia. Except for the upper parts, covellite is practically absent eastwards, in the breccia with clasts of the metasedimentary rock (Fig. 13). Enargite and native sulfur are widespread in the central heterolithic and jigsaw breccias. Eastward, native sulfur occurs along the altered and brecciated Trampeadero porphyry without enargite, whereas enargite is widespread in the

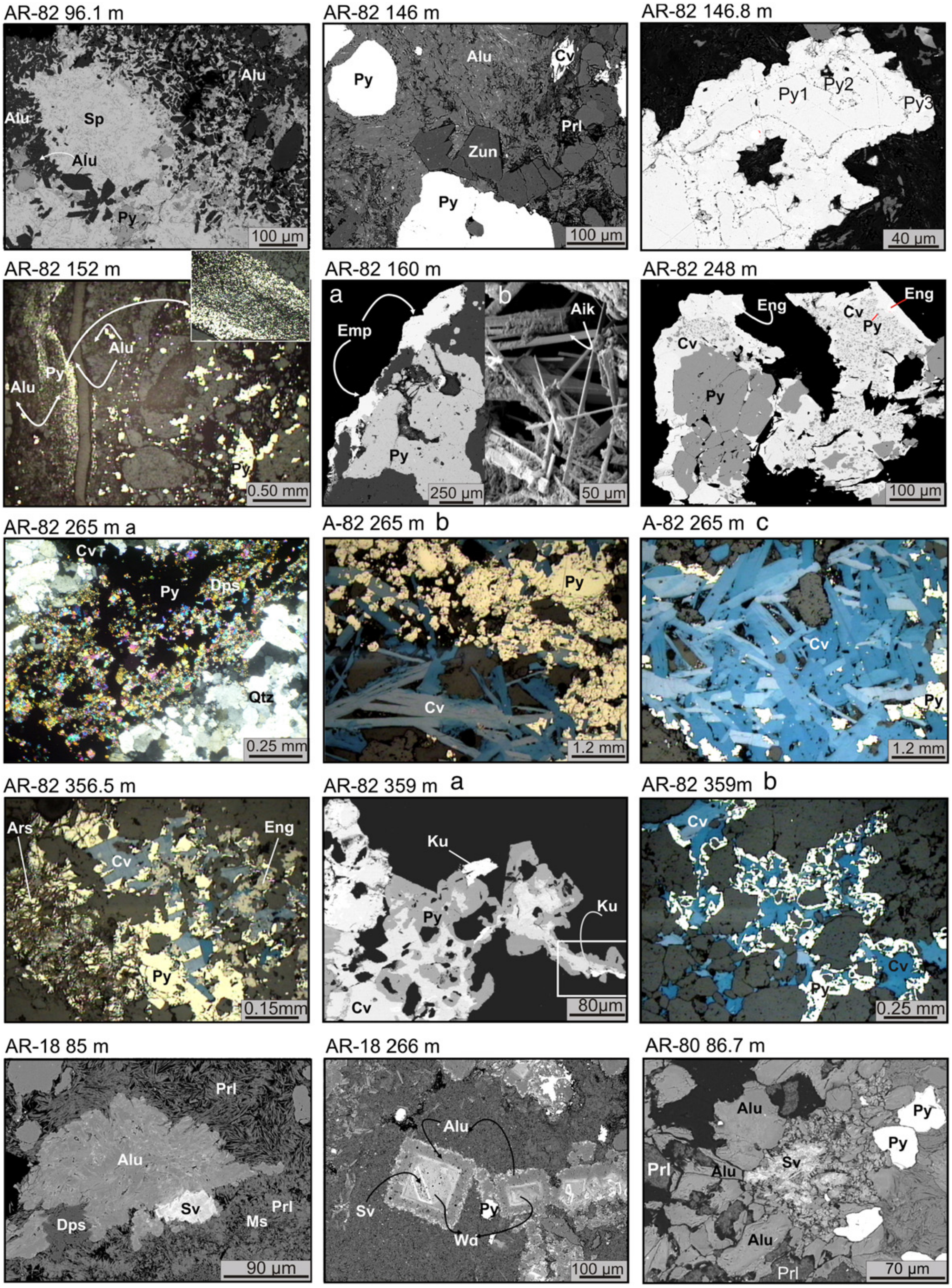

Fig. 14. Photomicrographs and SEM-BSE images illustrating examples of the advanced argillic alteration mineralogy, their microscopic arrangement, and textures. AR-82 96.1 m: A sphalerite veinlet cuts alunite + pyrite hydrothermal cement of the matrix-supported heterolithic breccia. AR-82 146 m: alunite + pyrite + zunyite hydrothermal cement of the matrix-supported heterolithic breccia with remnants of pyrophyllite (as rock flour). AR-82 146.8 m: three generations of pyrite. AR-82 152 m: fine-grained pyrite veinlet (enlarged) cut by a late alunite veinlet; to the right, early, coarser grained pyrite fragments and cement of the heterolithic breccia. AR-82 160 m a Emplectite rimming pyrite and b detail of a vug with aikinite needles in the same sample. AR-82 248 m: Pyrite is rimmed by covellite that contains numerous micro inclusions of pyrite and enargite rims covellite. AR-82 265 m a) Diaspore + sulfides cementing the clast-supported hydrothermal breccia. AR-82 265 m b) Early pyrite rimmed by a second pyrite generation and euhedral covellite plates. AR-82 265 m c) Detail of covellite crystal aggregates in the Cu-richest zone of the heterolithic breccia. AR-82 356.5 m: Covellite + pyrite + enargite and arsenopyrite (in sectors rims pyrite) cement in the jig saw breccia. AR-82 359 m a) Pyrite and kuramite rims covellite cement of the jig saw breccia. AR-82 359 m b) Covellite crystal aggregates rimmed by late, fine-grained pyrite. AR-18 85 m: Clots of alunite + svanvergite + diaspore in altered porphyry clast (with pyrophyllite and remnants of white mica), monolithic breccia. AR-18 266 m: euhedral, trapezoedric svanbergite and pseudocubic woodhouseite rimmed by alunite in the altered Trampeadero porphyry. AR-80 86.7 m: micro-inclusions of svanvergite in alunite and pyrite cementing monolithic breccias with previous pyrophyllite. Aik = aikinite; Alu = alunite; Ars = arsenopyrite; Cv = covellite; Dsp = diaspore; Emp = emplectite; Eng = enargite; Ku = kuramite; Prl = pyrophyllite; Py = pyrite; Qtz = quartz; Sp = sphalerite; Sv = svanbergite; Wd = woodhouseite; and Zun = zunyite.

Table 2
Chemical compositions of phyllosilicates in the potassic and phyllic alteration zones.

Phyllosilicate alteration sample N° (wt.%)	Biotite							White micas							
	Potassic							Phyllic							
	AR9-166 m							AR9-90.6 m	AR9-166 m	AR9-264 m	AR82-552 mm	AR82-655 m	AR18-39 m	AR18-266 m	AR18-2496 m
SiO_2	38.63	36.97	37.44	36.21	36.14	38.88	36.14	48.52	49.75	50.60	48.40	46.93	48.20	47.59	46.95
TiO_2	2.17	2.18	1.69	1.70	1.40	2.29	2.60	0.25	0.07	0.05	0.45	0.40	0.01	0.29	0.00
Al_2O_3	16.04	17.41	17.40	19.06	18.83	15.33	18.64	37.77	35.35	35.62	33.07	35.60	34.69	35.68	35.98
[a]FeO	11.14	11.96	12.02	12.20	8.98	10.48	11.68	0.21	1.51	0.88	0.34	0.11	1.75	0.75	0.74
MnO	0.07	0.08	0.08	0.16	0.10	0.13	0.18	0.00	0.00	0.02	0.00	0.00	0.00	0.07	0.01
MgO	17.98	16.93	17.48	15.05	17.61	18.15	16.05	1.30	1.29	0.91	1.85	1.88	0.89	0.45	0.48
CaO	0.00	0.00	0.01	0.00	0.00	0.00	0.00	0.00	0.13	0.18	0.05	0.03	0.06	0.03	0.00
SrO	0.05	0.05	0.05	0.04	0.04	0.05	0.08	0.06	0.08	0.06	0.06	0.05	0.11	0.06	0.10
BaO	0.14	0.08	0.00	0.00	0.05	0.10	0.00	0.16	0.01	0.08	0.06	0.17	0.02	0.21	0.16
Na_2O	0.12	0.13	0.11	0.09	0.11	0.18	0.09	0.25	0.07	0.06	0.10	0.11	0.22	0.25	0.34
K_2O	9.81	9.85	9.56	9.64	9.83	9.66	9.75	9.70	7.33	6.58	9.89	9.65	9.43	7.58	9.46
F	4.15	3.61	3.56	3.40	3.52	4.38	3.11	1.31	0.45	0.00	1.12	0.16	0.63	0.17	0.23
Cl	0.24	0.23	0.21	0.19	0.16	0.24	0.25	0.00	0.01	0.03	0.04	0.00	0.03	0.01	0.01
P_2O_5	0.02	0.00	0.00	0.00	0.02	0.00	0.01	0.07	0.03	0.11	0.00	0.02	0.11	0.06	0.09
Total	98.75	97.90	98.05	96.27	95.28	97.97	97.23	99.05	95.88	95.16	94.94	95.05	95.89	93.12	94.46
Number of cations for $O_{20}(OH)_4$															
T-site															
^{IV}Si	5.37	5.23	5.27	5.20	5.38	5.68	5.15	6.10	6.40	6.52	6.43	6.19	6.32	6.32	6.24
^{IV}Al	2.63	2.78	2.73	2.80	2.62	2.32	2.85	1.90	1.60	1.48	1.57	1.81	1.68	1.68	1.76
M-site															
^{VI}Al	0.00	0.13	0.15	0.42	0.68	0.32	0.28	3.70	3.77	3.92	3.62	3.73	3.68	3.91	3.87
^{VI}Ti	0.23	0.23	0.18	0.18	0.16	0.25	0.28	0.02	0.01	0.00	0.04	0.04	0.00	0.03	0.00
Fe	1.30	1.41	1.41	1.46	1.12	1.28	1.39	0.02	0.16	0.09	0.04	0.01	0.19	0.08	0.08
Mn	0.01	0.01	0.01	0.02	0.00	0.00	0.02	0.00	0.00	0.00	0.00	0.00	0.00	0.01	0.00
Mg	3.73	3.57	3.67	3.22	3.90	3.95	3.41	0.24	0.25	0.18	0.37	0.37	0.17	0.09	0.10
A-site															
Ca	0.00	0.00	0.00	0.00	0.00	0.00	0.00	0.00	0.02	0.01	0.00	0.01	0.01	0.01	0.00
Na	0.03	0.04	0.03	0.03	0.03	0.05	0.02	0.06	0.02	0.01	0.03	0.03	0.06	0.06	0.09
K	1.74	1.78	1.72	1.77	1.87	1.80	1.77	1.56	1.20	1.08	1.68	1.62	1.58	1.28	1.60
Ba	0.01	0.00	0.00	0.00	0.00	0.00	0.00	0.00	0.00	0.02	0.01	0.00	0.00	0.00	0.00
SrO	0.00	0.00	0.00	0.00	0.00	0.00	0.00	0.01	0.00	0.00	0.00	0.00	0.01	0.00	0.01
OH-site															
F	1.82	1.61	1.58	1.54	1.48	1.88	1.40	0.52	0.18	0.00	0.47	0.07	0.26	0.07	0.10
Cl	0.06	0.06	0.05	0.05	0.04	0.06	0.06	0.00	0.01	0.01	0.01	0.00	0.01	0.00	0.00
OH	2.12	2.33	2.37	2.41	2.48	2.06	2.54	3.48	3.82	3.99	3.52	3.93	3.73	3.93	3.90

[a] Iron as Fe^{2+} for biotite and as Fe^{3+} for white micas.

breccia with clasts of the metasedimentary rock and at deeper levels, as veinlets cutting the phyllic alteration without native sulfur (Fig. 13). Enargite compositions varies from the typical enargite chemical formula with low Sb substitution for As (0–0.52% Sb), Sn–V enargite (0.87% V–0.45% Sn), and colusite with V (2.95–3.13% V) and Sn (4.61–6.60% Sn) lithophile element substitution (Table 4). Other analyzed sulfides (see Table 4) include kuramite, located in the jigsaw breccia, late, low iron (0–0.51% Fe) sphalerite veinlets in the upper levels of the heterolithic breccia, colucite, emplectite, and aikinite as needles filling cavities.

9. Fluid inclusion systematics

Preliminary fluid inclusion studies have been conducted on selected samples with minimal evidence of the overprinting of later hydrothermal stages.

A-type quartz veinlets in the Seca Norte porphyry with potassic patches (AR-9 223 m; Fig. 9b) contain two main groups of fluid inclusions. The first group consists of brine inclusions and vapor rich inclusions without evidence of CO_2 and some (very few) empty inclusions (they probably have lost their contents during the crystal fracturing). In the polyphase brine inclusions, the solids (generally one or two) are pseudocubic (halite) and a rare amorphous compound. The bubble occupies >10% of the inclusion volume. The eutectic temperatures range between −60 and −50 °C, suggesting the presence of Ca^{2+} in the solution. They homogenize by bubble expansion to the vapor phase at temperatures varying from 355 to 455 °C. Halite dissolved at temperatures between 425 and 460 °C, indicating a salinity >50 wt.% NaCl equiv. The second group of fluid inclusions are vapor-rich fluid inclusions and brine inclusions aligned along fractures in quartz and of uncertain association (secondary?). The former has an aqueous-carbonic composition (the carbonic phase occupies between 30 and 50% of the fluid inclusion). The temperatures of melting CO_2 (−63° to −61 °C) suggest that in the carbonic phase there are other molecular compounds besides CO_2. Laser Raman detected CO_2 and H_2S in a few analyzed fluid inclusions. Last melting of clathrate occurred at 3 and 5 °C, indicating salinities of 12 and 15 wt.% NaCl equiv. The homogenization temperatures of CO_2 (between 26 and 30 °C, to the vapor phase) suggest densities lower than 0.25 g/cm^3 for these fluids. Total homogenization temperatures measured in some inclusions were always higher than 400 °C. The associated polyphase brine fluid inclusions contain unidentified (non-cubic) solids ± triangular chalcopyrite ± red hematite. The bubble occupies less than 20% of the total volume of the fluid inclusion cavity. Their eutectic temperature was very low (−53 °C), suggesting the presence of Ca^{2+} in the solution. The temperature of melting ice was −16 to −15 °C. They homogenize to the vapor phase at 400 °C and between 450 and >500 °C (Th liquid–vapor). It was not possible to verify the temperature of dissolution of non-cubic crystals.

B-type quartz veinlets in the Seca Norte porphyry with phyllic alteration (AR-9 324 m) contain two main types of primary fluid inclusions. The most abundant are vapor-rich fluid (between 75 and 90% vapor) inclusions that homogenize to the vapor at 400 °C and at 450–>500 °C. The polyphase brine inclusions contain halite, rarely other daughter crystal (sylvite?), and opaques (triangular chalcopyrite and an unknown phase). These inclusions homogenize to the

Table 3

Representative chemical compositions of andalusite, pyrophyllite, diaspore, zunyite, and alunite-group minerals in the advance argillic alteration zone.

Mineral (wt.%)	Andalusite			Pyrophyllite			Diaspore			Zunyite			Alunite			Svanvergite			Woodhouseite		
	AR9-264 m	AR18-249 m	AR18-249 m	AR82-96 m	AR18-85 m	AR80-86 m	AR82-333 m	AR18-266 m	AR18-266 m	AR82-96 m	AR80-86 m	AR80-160 m	AR82-160 m	AR18-85 m	AR80-86 m	AR82-146 m	AR18-85 m	AR80-86.7 m	AR18-266 m	AR18-266 m	AR18-266 m
SiO_2	34.93	35.64	36.38	65.70	67.33	66.01	0.12	0.16	0.27	22.13	23.10	23.19	0.00	0.00	0.00	0.00	0.00	0.00	0.00	0.00	0.00
TiO_2	0.22	0.28	0.02	0.03	0.04	0.00	0.00	0.00	0.00	0.04	0.00	0.00	0.00	0.00	0.00	0.00	0.00	0.00	0.00	0.00	0.00
Al_2O_3	64.57	64.52	62.90	29.47	28.17	28.04	83.57	83.09	80.62	56.96	56.89	55.20	41.12	36.90	41.19	31.41	38.02	31.32	31.87	30.82	32.78
[a]FeO	0.23	0.26	0.63	0.00	0.05	0.19	0.00	0.14	0.06	0.01	0.00	0.00	0.00	0.07	0.00	0.00	0.06	0.00	0.00	0.07	0.00
MnO	0.00	0.00	0.00	0.03	0.00	0.00	0.00	0.00	0.00	0.00	0.00	0.00	0.00	0.00	0.00	0.00	0.00	0.00	0.00	0.00	0.00
MgO	0.05	0.06	0.05	0.01	0.01	0.01	0.00	0.00	0.00	0.00	0.00	0.00	0.00	0.00	0.06	0.00	0.00	0.00	0.00	0.00	0.00
CaO	0.00	0.00	0.00	0.01	0.02	0.04	0.20	0.00	0.01	0.00	0.00	0.00	0.00	0.50	0.00	0.57	3.36	1.61	9.64	7.19	8.65
SrO	0.00	0.00	0.00	0.10	0.04	0.09	0.00	0.00	0.00	0.00	0.00	0.00	0.41	1.28	1.10	17.34	7.97	4.88	1.81	3.20	3.31
BaO	0.00	0.00	0.00	0.19	0.08	0.04	0.00	0.00	0.00	0.00	0.00	0.00	0.00	0.00	0.00	0.00	0.00	0.00	0.00	0.00	0.00
Na_2O	0.00	0.00	0.00	0.09	0.13	0.06	0.00	0.00	0.00	0.02	0.00	0.00	0.42	0.47	0.18	0.14	0.05	0.13	0.10	0.09	0.00
K_2O	0.00	0.02	0.02	0.07	0.12	0.04	0.02	0.02	0.01	0.00	0.00	0.00	6.09	4.34	0.00	0.12	0.57	0.64	0.05	0.13	0.00
F	0.00	0.00	0.00	0.31	0.38	0.24	0.00	0.00	0.00	8.49	3.77	5.43	0.00	0.00	0.00	0.00	0.00	0.00	0.00	0.00	0.00
Cl	0.00	0.00	0.00	0.00	0.13	0.03	0.00	0.00	0.00	2.65	2.78	2.87	0.00	0.00	0.00	0.00	0.00	0.00	0.00	0.00	0.00
P_2O_5	0.00	0.00	0.00	0.00	0.02	0.00	0.00	0.06	0.04	1.07	0.00	0.86	0.44	1.79	0.05	13.75	16.54	12.66	18.08	14.84	19.79
SO_3	0.00	0.00	0.00	0.00	0.00	0.00	0.00	0.00	0.02	0.00	0.00	0.00	39.29	32.46	37.54	17.84	8.63	25.91	11.99	14.51	10.50
Total	100.00	100.78	100.00	95.88	96.32	94.69	83.91	83.47	81.03	94.41	86.54	87.55	87.77	77.81	85.71	81.17	75.14	77.21	73.54	70.85	75.03
	5 (O)			O20(OH)4			2 (O, OH)			38 (O, OH, F)			11 (O, OH)			14 (O, OH)			14 (O, OH)		
Si	0.95	0.96	0.99	7.86	8.01	7.98	0.01	0.00	0.00	5.16	5.66	5.62	0.00	0.00	0.00	0.00	0.00	0.00	0.00	0.00	0.00
Al	2.06	2.04	2.01	4.16	3.96	4.00	1.33	1.33	1.33	15.66	16.43	15.77	3.20	3.26	3.30	3.82	4.82	3.55	3.95	3.96	4.02
Ti	0.00	0.01	0.00	0.00	0.00	0.00	0.00	0.00	0.00	0.01	0.00	0.00	0.00	0.00	0.00	0.00	0.00	0.00	0.00	0.00	0.00
Fe	0.01	0.01	0.01	0.00	0.00	0.01	0.00	0.00	0.00	0.00	0.00	0.00	0.00	0.00	0.00	0.00	0.01	0.00	0.00	0.01	0.00
Mn	0.00	0.00	0.00	0.00	0.00	0.00	0.00	0.00	0.00	0.00	0.00	0.00	0.00	0.00	0.00	0.00	0.00	0.00	0.00	0.00	0.00
Mg	0.00	0.00	0.00	0.00	0.00	0.00	0.00	0.00	0.00	0.00	0.00	0.00	0.00	0.00	0.01	0.00	0.00	0.00	0.00	0.00	0.00
Ca	0.00	0.00	0.00	0.01	0.01	0.00	0.00	0.00	0.00	0.00	0.00	0.00	0.00	0.04	0.00	0.06	0.38	0.17	1.09	0.84	0.96
Sr	0.00	0.00	0.00	0.00	0.00	0.01	0.00	0.00	0.00	0.00	0.00	0.00	0.02	0.06	0.04	1.04	0.50	0.27	0.11	0.20	0.20
Ba	0.00	0.00	0.00	0.00	0.00	0.00	0.00	0.00	0.00	0.00	0.00	0.00	0.00	0.00	0.00	0.00	0.00	0.00	0.00	0.00	0.00
Na	0.00	0.00	0.00	0.02	0.03	0.03	0.00	0.00	0.00	0.01	0.00	0.00	0.05	0.07	0.02	0.03	0.01	0.02	0.02	0.02	0.00
K	0.00	0.00	0.00	0.01	0.02	0.01	0.00	0.00	0.00	0.00	0.00	0.00	0.51	0.42	0.48	0.02	0.08	0.08	0.01	0.02	0.00
F	0.00	0.00	0.00	0.12	0.14	0.05	0.00	0.00	0.00	6.26	2.92	4.16	0.00	0.00	0.00	0.00	0.00	0.00	0.00	0.00	0.00
Cl	0.00	0.00	0.00	0.00	0.03	0.01	0.00	0.00	0.00	1.05	1.15	1.18	0.00	0.00	0.00	0.00	0.00	0.00	0.00	0.00	0.00
P	0.00	0.00	0.00	0.00	0.00	0.00	0.00	0.00	0.00	0.21	0.00	0.18	0.02	0.11	0.00	1.20	1.50	1.03	1.61	1.37	1.74
S	0.00	0.00	0.00	0.00	0.00	0.00	0.00	0.00	0.00	0.00	0.00	0.00	1.95	1.83	1.91	1.38	0.70	1.87	0.95	1.19	0.82

[a] All Fe as Fe^{3+}.

Table 4
Chemical compositions of sulfides in the Advance Argillic Alteration zone.

Sulfide alteration type (wt.%)	Pyrite			Pyrite			Pyrite			Pyrite			Covellite		
	Heterolithic breccia			Heterolithic breccia			Monolithic breccia			Alunite + pyrite			Heterolithic breccia		
	Clast supported			Matrix supported			Clast supported			Veinlets, clots			Clast supported		
				Core	Rim	Rim									
S	52.76	51.99	52.81	53.07	52.75	52.83	52.82	53.23	53.42	54.50	54.30	54.30	33.29	33.87	34.02
V	0.00	0.00	0.05	0.00	5.00	0.08	0.06	0.08	0.00	0.00	0.00	0.00	0.00	0.00	0.00
Fe	46.47	45.03	46.15	46.42	45.83	45.33	45.75	45.57	45.83	46.01	46.25	46.25	0.00	0.03	0.00
Cu	0.00	2.08	0.00	0.00	0.17	0.44	0.30	0.00	0.00	0.29	0.06	0.06	66.34	65.49	65.39
Zn	0.47	0.84	0.64	0.51	0.71	1.32	0.70	0.54	0.46	0.00	0.05	0.05	0.15	0.00	0.00
As	0.24	0.06	0.10	0.00	0.10	0.00	0.13	0.15	0.06	0.00	0.00	0.00	0.00	0.00	0.00
Ag	0.00	0.00	0.00	0.00	0.00	0.00	0.00	0.00	0.00	0.00	0.00	0.00	0.00	0.00	0.00
Sn	0.07	0.00	0.15	0.00	0.17	0.00	0.10	0.24	0.23	0.00	0.00	0.00	0.22	0.00	0.00
Sb	0.00	0.00	0.11	0.00	0.23	0.00	0.15	0.19	0.00	0.00	0.00	0.00	0.00	0.00	0.00
Au	0.00	0.00	0.00	0.00	0.00	0.00	0.00	0.00	0.00	0.00	0.05	0.05	0.00	0.00	0.00
Mo	0.00	0.00	0.00	0.00	0.00	0.00	0.00	0.00	0.00	0.00	0.00	0.00	0.00	0.00	0.00
Bi	0.00	0.00	0.00	0.00	0.00	0.00	0.00	0.00	0.00	0.00	0.00	0.00	0.00	0.00	0.00
Total	100.01	100.00	100.01	100.00	104.96	100.00	100.01	100.00	100.00	100.80	100.71	100.71	100.00	99.39	99.41

Sulfide alteration type (wt.%)	Covellite			Covellite			Covellite			Enargite			Enargite		
	Heterolithic breccia			Monolithic breccia			Alunite + pyrite + covellite			Heterolithic breccia			Monolithic breccia		
	Matrix supported			Clast supported			Veinlets, clots			Clast supported			Clast supported, jig-saw		
S	34.06	33.97	33.06	33.75	33.52	33.61	33.92	33.95	33.61	31.81	32.68	32.40	32.85	32.58	32.71
V	0.02	0.01	0.00	0.00	0.05	0.00	0.00	0.00	0.00	0.87	0.00	0.02	0.00	0.00	0.00
Fe	0.66	0.68	0.63	0.49	0.16	0.00	0.10	0.05	0.05	0.85	0.17	0.02	0.26	0.00	0.13
Cu	65.79	66.18	65.80	65.67	65.38	66.07	65.44	64.89	65.25	48.80	49.26	48.71	49.37	48.72	48.55
Zn	0.00	0.00	0.31	0.00	0.00	0.00	0.00	0.00	0.00	0.60	0.00	0.00	0.34	0.00	0.17
As	0.05	0.00	0.05	0.00	0.00	0.00	0.00	0.00	0.00	16.12	17.37	18.85	18.74	17.71	18.22
Ag	0.00	0.00	0.00	0.00	0.00	0.01	0.00	0.00	0.00	0.00	0.00	0.00	0.00	0.00	0.00
Sn	0.00	0.00	0.14	0.02	0.00	0.00	0.00	0.00	0.00	0.45	0.00	0.00	0.00	0.00	0.00
Sb	0.00	0.00	0.00	0.00	0.00	0.00	0.00	0.00	0.00	0.50	0.52	0.29	0.09	0.00	0.04
Au	0.00	0.00	0.00	0.00	0.06	0.03	0.00	0.09	0.10	0.00	0.00	0.00	0.00	0.00	0.00
Mo	0.00	0.00	0.00	0.00	0.00	0.00	0.00	0.00	0.00	0.00	0.00	0.00	0.00	0.00	0.00
Bi	0.00	0.00	0.00	0.00	0.00	0.00	0.00	0.00	0.00	0.00	0.00	0.00	0.00	0.00	0.00
Total	100.57	100.84	99.99	99.93	99.17	99.72	99.46	98.98	99.01	100.00	100.00	100.28	101.64	99.01	99.82

Sulfide alteration type	Molybdenite			Sphalerite			Emplectite			Kuramite			Colusite		
	Breccias			Heterolithic breccia			Heterolithic breccia			Monolithic breccia			Heterolith breccia		
				Matrix supported			Matrix supported			Jig zaw			Matrix supported		
S	42.10	42.51		33.52	31.25	31.33	21.13	21.04	21.31	33.02	33.14		31.75	31.13	
V	0.00	0.00		0.02	0.00	0.00	0.00	0.00	0.00	0.00	0.00		3.13	2.95	
Fe	0.08	0.00		0.51	0.00	0.00	0.10	0.20	0.03	0.00	0.00		0.08	0.28	
Cu	0.20	0.03		0.07	0.00	0.00	19.30	19.07	19.28	44.04	44.09		49.96	49.71	
Zn	0.11	0.00		66.32	68.60	68.29	0.00	0.12	0.11	0.00	0.00		0.01	0.00	
As	0.06	0.00		0.00	0.15	0.18	0.00	0.00	0.00	0.00	0.00		9.71	8.96	
Ag	0.00	0.00		0.04	0.00	0.00	0.00	0.00	0.00	0.00	0.00		0.00	0.00	
Sn	0.00	0.00		0.00	0.00	0.20	0.00	0.00	0.00	23.28	23.20		4.61	6.60	
Sb	0.00	0.00		0.01	0.00	0.00	0.00	0.00	0.00	0.00	0.00		0.00	0.00	
Au	0.00	0.00		0.07	0.00	0.00	0.00	0.00	0.00	0.00	0.00		0.00	0.00	
Mo	58.44	56.56		0.00	0.00	0.00	0.00	0.00	0.00	0.00	0.00		0.00	0.00	
Bi	0.00	0.00		0.00	0.00	0.00	60.41	60.31	60.15	0.00	0.00		0.00	0.00	
Total	100.99	99.10		100.56	100.00	100.00	100.94	100.74	100.88	100.34	100.43		99.24	99.62	

liquid at temperatures >500 °C and halite dissolves between 245 and 290 °C, corresponding to salinities between 35 and 38 wt.% NaCl equiv.

A similar fluid inclusion assemblage was observed in B-type quartz veinlets in the Trampeadero porphyry with phyllic alteration and incipient advanced argillic alteration (AR-18 207 m), except that the proportion of polyphase inclusions is minor; rather, they contain polyphase aqueous liquid inclusions (some with opaque daughter phases) and vapor-rich inclusions have homogenization temperatures between 375 and 500 °C (ThL) and 390–500 °C (ThV), respectively, only a few FIA homogenized at temperatures >500 °C. No microthermometric measurements have been reported for fluid inclusions in B-type veinlets in the metasedimentary rock with phyllic alteration (AR-82 624 m), but aqueous liquid inclusions dominate over vapor and polyphase inclusions. In the silicified groundmass of the Seca Norte porphyry with phyllic alteration (AR-9 90.6 m), there is also a population of aqueous liquid inclusions.

10. Discussion

The polymetallic Agua Rica deposit is a telescoped system in which the alteration mineralogy of deep, intermediate, and shallow events are now exposed together at the same level of erosion. In the E–W 6969400 section examined, two of the three main hydrothermal stages have been identified and consist of the porphyry (deeper) and the epithermal (intermediate level) stages. A shallow barren crater infill breccia (Fig. 1; see Landtwing et al., 2002) has not been intersected by this section.

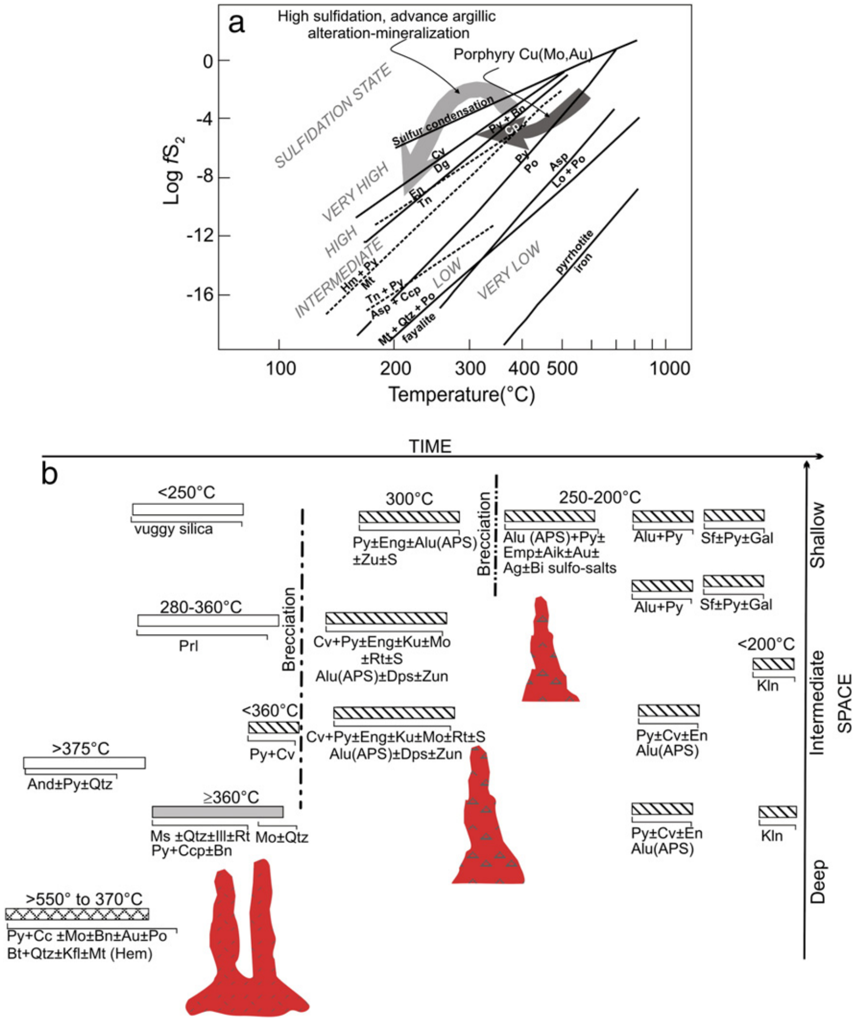

Fig. 15. a) $f(S_2)$ versus temperature showing hydrothermal fluids evolution in the Agua Rica deposit. The dark gray arrow named porphyry Cu (Mo, Au) shows the initial assemblages of low to intermediate sulfidation deposited at approximately at >500–370 °C and culminated with high sulfidation assemblage of the phyllic alteration (~350 °C). The light gray arrow indicates the high sulfidation assemblages deposited before and after brecciation (modified from Einaudi et al., 2003 and references therein). b) Schematic time–space diagram summarizing alteration–mineralization assemblages of the porphyry and high sulfidation advanced argillic stages and estimated temperatures. See text for explanation. Aik = aikinite; Alu = alunite; And = andalusite; APS = woodhouseite, svanvergite; Ars = arsenopyrite; As = arsenopyrite; Bn = bornite; Bt = biotite; Cv = covellite; Dg = digenite; Dsp = diaspore; Emp = emplectite; Eng = enargite; Gal = galena; Hem = hematite; Ill = illite: Ku = kuramite; Lo = loellingite; Mo = molybdenite; Mt = magnetite; Po = pyrrhotite; Prl = pyrophyllite; Py = pyrite; Qtz = quartz; Sf = sphalerite; Tn = Tennantite; and Zun = zunyite.

Early potassic alteration patches and A- and B-type veinlets are preserved in the Seca Norte porphyry, which contains moderate hypogene Cu and Au grades (Fig. 11). In contrast, only B-type quartz veins are observed in the Trampeadero Porphyry, which is Mo-rich and Cu- and Au-depleted when compared with Seca Norte (Fig. 11). Preliminary fluid inclusion results from A-type quartz veinlets indicate the presence of complex fluids, the coexistence of vapor and hypersaline fluids during this early porphyry stage and a wide range of homogenization temperatures (ThL-V). Salinity and homogenization temperatures are slightly lower for the fluid inclusions in the B-type quartz veinlets in the Seca Norte and Trampeadero prophyries. They also show that the major salt components in magmatic fluids are NaCl, KCl, and $CaCl_2$ (in hypersaline magmatic liquids), ore metals (as indicated by chalcopyrite, hematite, and other unidentified opaque daughter minerals) and volatiles, such CO_2 and sulfur species, as indicated by CO_2 and H_2S in vapor inclusions. These volatiles were observed in other porphyry-related and epithermal fluid inclusions (Redmond et al., 2004; Ronacher et al., 2004). The association of primary multisolid and vapor-rich fluid inclusions in A-type quartz veinlets is interpreted to have been formed when a supercritical magmatic fluid decompressed and cooled and intersected the solvus (Cline, 1995). These orthomagmatic fluids are the precursors of the early sulfide-oxide assemblages (pyrite + chalcopyrite + molybdenite ± bornite ± pyrrhotite; pyrite + magnetite (± hematite) + chalcopyrite; BHP, 1999) and gold deposited at intermediate sulfidation states (Fig. 15; Einaudi et al., 2003). Recent studies (William-Jones and Heinrich, 2005) show the preference of Cu and Au to be partitioned and transported by a vapor phase (or its derived fluids) that also contains a significant proportion of the exsolved sulfur. The magmas of the Farallón NegroVolcanic Complex that formed the Bajo de la Alumbrera porphyry Cu–Au deposit and the Agua Rica deposit are exceptionally high in sulfur (see Halter et al., 2005).

The Trampeadero porphyry and the metasedimentary rock in the section display B-type veinlets with molybdenite (or molybdenite stringers) and pervasive phyllic alteration accompanied by disseminated, very fine-grained pyrite and covellite that replace pre-existing grains of pyrrhotite, chalcopyrite, and bornite as indicated by their inclusions or remnants within pyrite and covellite. Based on metal grades (Fig. 11), this stage did not add Cu, Au, and As, but some of the stockwork quartz veinlets have apparently been striped/leached of their former sulfides and iron oxide content during the phyllic overprinting process. The mineralogy and textures of the phyllic halo suggest the influence of at least two different environments. Cooling of hydrothermal fluids that expanded outward and upwards from the potassic alteration zones in both porphyries may have caused the biotite breakdown to white micas and rutile, as well as K-feldspar replacement. Evidence of dominant aqueous liquid over vapor-rich or multiphase in the phyllic halo was observed in quartz veinlets in the altered metasedimentary rock (AR-82 624 m) and in the Seca Norte porphyry (AR-9 90.6 m). In the Seca Norte porphyry and in other sections of the deposit, the influence of the superposed hydrothermal breccias is more localized; the phyllic halo preserves pyrite, chalcopyrite, and bornite mineralization, as well as molybdenite, accompanying white micas and rutile. Thus, in the analyzed section, due to telescoping the low to intermediate sulfidation chalcopyrite and bornite assemblage seems to have been reconstituted as high sulfidation covellite and any early iron oxide may have been transformed into pyrite, which also has encapsulated chalcopyrite, pyrrhotite, and bornite. Hydrothermal fluids may have achieved a very high sulfidation state at temperatures near 350 °C (Fig. 15; Einaudi et al., 2003), and high ratio of H_2S/Fe that prevented deposition of Au with Cu–Fe sulfides (Williams-Jones and Heinrich, 2005). Also, the textural record of dissolution of ore minerals preserved in early veinlets was probably common in such an environment with fluctuating fluid conditions.

High Mo grades are in the Trampeadero porphyry and in the surrounding metasedimentary rock as quartz + molybdenite veinlets and (or) molybdenite stringers (Figs. 2c and 11). These grades are much higher than Mo grades in the Seca Norte porphyry. If both porphyries were derived from a common parent magma, then the magma could have underwent some degree of crystallization prior to the Trampeadero intrusion, and Mo, as an incompatible element, could have become enriched in the residual melt (see Candela and Holland, 1986; Robb, 2005; Stemprok, 1990) rather than a slightly deeper setting or lower initial water content for the Trampeadero porphyry, which were arguments used to explain the origin of porphyry Mo-(Cu) relative to porphyry Cu-(Mo) (Candela and Holland, 1986; Woodcock and Hollister, 1978). Once Mo partitioned in the hydrothermal fluids, the abundance of sulfur in the Agua Rica hydrothermal system and cooling of fluids could have favored its precipitation as molybdenite in equilibrium with white micas (Cao, 1989; Gu, 1993; Tingle and Fenn, 1984; Ulrich and Mavrogenes, 2008; Wood et al., 1987). In the Bajo de la Alumbrera porphyry Cu deposit, the Mo distribution is also not correlated with Cu or Au grades and the deposition of molybdenite is peripheral to and slightly later than the precipitation of Cu and Au (Ulrich and Heinrich, 2001). In the porphyry Cu–Mo deposit at Butte, molybdenite mineralization in quartz-dominated veins also occurred by a different mechanism than Cu, but probably was driven by a pressure decrease rather than cooling (Rusk et al., 2008). In a recent investigation of the giant Questa porphyry Mo deposit, Klemm et al. (2008) found that molybdenite precipitation occurred by cooling of a Mo enriched (~500 ppm), but Cu depleted, residual brine from 420 °C to 350 °C.

The presence of local monomineralic andalusite or andalusite ± quartz ± pyrite lenses in the root zones of the advanced argillic alteration envelope with K feldspar, may represent the earliest and deepest, high-temperature advanced argillic assemblage (Fig. 15; Hemley et al., 1980). Clasts of the Trampeadero porphyry and the metasedimentary rock with pervasive phyllic alteration, quartz veinlets, fine-grained pyrite–covellite disseminations, and molybdenite are well preserved in the monolithic breccia types located east of the section, thus brecciation clearly postdated the porphyry stage (at this level), the hypogene reconstitution of sulfides from the early porphyry stage and andalusite formation. Likewise, in these clasts pyrophyllite replaces white micas from the phyllic assemblage, indicating that its formation also predates brecciation. In the central heterolithic breccia, pyrophyllite occurs with other minerals of the advanced argillic assemblage in the matrix, but in contrast to these minerals that clearly replace the matrix, it is brownish and turbid (could be part of the matrix). The assemblage andalusite at depth and pyrophyllite at higher elevations is considered part of this early advanced argillic alteration stage formed from very acidic fluids probably originating during the absorption of early spent porphyry ore fluids, which had expanded to a low-density vapor, by heated ground water (see Williams-Jones and Heinrich, 2005). In the central and upper part of the section, these very acid waters may have precipitated silica and leached all previous alteration minerals leaving only vuggy quartz that were preserved as clasts in the heterolithic hydrothermal breccia, between 10 and 200 m depth (Fig. 4). The absence of residual silica in the other breccias localized east of the section or in other sectors of the advanced argillic alteration halo (Figs. 5 and 7), probably is indicating the neutralization of the acidic fluids during its interaction with wall rocks, although the upper levels of these breccias underwent greater erosion (Fig. 2b). In this early stage of the advanced argillic alteration, hydrothermal fluids seems to have not precipitated sulfides or sulfosalts, thus, it has not contributed Cu and Au to the total metal content of the Agua Rica system. Nevertheless, there are textural evidences of remobilization of early sulfides, like molybdenite, and also early sulfides could have undergone dissolution. In conclusion to the previous observation that brecciation post-dated stockwork-veined, potassically altered and mineralized porphyries (Landtwing et al., 2002), this study indicates that the phyllic alteration of porphyries and host rocks with reconstitution of early sulfides to pyrite and covellite, and an early stage of advanced argillic alteration also predates the main hydrothermal brecciation stage (at this structural level).

Subsequent hydrothermal brecciation was probably driven by unroofing associated with release of mechanical energy due to fluid expansion, exsolved from a new shallowly emplaced magma (see Landtwing et al., 2002) with magmatic fluids responsible for producing and precipitating intermediate temperature advanced argillic paragenesis (alunite (svanbergite ± woodhouseite) ± diaspore ± zunyite) as breccia cement accompanied by Fe–Cu–As–Sn–S, Fe–Au–Ag–Bi–S, and Zn–Pb–S mineralization. The distribution of these advanced argillic alteration minerals and the lack of a strong hydrothermal overprint on much of the Seca Norte porphyry, the least-altered zone (Fig. 2b), suggests that the granite breccia focused fluid flow during this post-early brecciation, high sulfidation epithermal event, as was previous noted by Landtwing et al. (2002). There is a zonation in the breccia styles along the section from heterolithic in the center to monolithic in the deeper central part and eastward. Textures vary also from jigsaw with angular rock fragments with minor displacement in the deepest central part, to clast-supported breccias with a matrix consisting predominantly of hydrothermal cement at intermediate depths in the center and eastward, to a matrix-supported breccia with rock flower (mixed tuffisite and cataclastite) and minor hydrothermal cement in the central zone, above 180 m depth and upwards. This last texture is a product of a high degree of mixing and milling of fragments, which indicates the highest zone of energy released of the examined breccias. The observed breccia texture in the heterolithic and monolithic breccias, and the complex cross-cutting relationships between hydrothermal breccia facies and igneous breccia (BHP, 1999) suggests that these processes may have been repeated several times during the protracted magmatic hydrothermal activity at Agua Rica; this supports that the deposit was forming in an environment of progressive decreasing paleodepth associated with degradation of the paleosurface (see also Landtwing et al., 2002), e.g., high erosion-exhumation rates. The sandy and pebble dikes cut the altered metasedimentary rock, the hydrothermal breccias, but also are brecciated and slightly mineralized. They are a type of intrusive breccia like the crater infill breccia exposed north of the section (Fig. 1c), interpreted to have been formed after hydrothermal breccias by shallow-level phreatomagmatic eruption involving preexisting rocks and juvenile magma (Landtwing et al., 2002). Nevertheless, these dikes are common in the area and occur as clasts in igneous, hydrothermal, and crater infill breccias and also cut all lithologies (see Landtwing et al., 2002); therefore they indicate prolonged escape of volatiles that are key to host rock preparation (cf. BHP, 1999).

This multistage high sulfidation epithermal event exhibits zonation in metals and sulfide minerals, mainly vertically, along the central heterolithic breccia from deeper levels proximal to the fluids source upwards and laterally from the heterolithic breccia to marginal monolithic breccia (Figs. 2c and 11). Iron is predominant in all zones. The Cu:Au ratios decrease from deeper parts of the breccia to higher levels, as does As. At shallow levels breccias are enriched in Pb, Zn with Au and Ag, nevertheless, Zn also occurs in deeper zones of the section as late mineralization. In general, the base-metals and Au decrease from the central zone eastward (Fig. 11). The zonation in the sulfide minerals reflects that of the ore metal distribution, based on assay data (Fig. 13). The precipitation of pyrite + covellite ± enargite ± molybdenite ± rutile or anatase ± kuramite, native sulfur, arsenopyrite with diaspore, alunite, and zunyite in this epithermal stage occurs in breccias (clast-supported breccia) at intermediate depth and in lateral transition zones to fractured and altered rocks (jigsaw breccia). Sulfides and gangue seem to have precipitated directly as cement between clasts, and in fractures that cut clasts, indicating pervasive fluid circulation and channeling through these breccia zones. This assemblage also suggests that at this stage hydrothermal fluids were oxidized and silica undersaturated, they had very high acidity (Giggenbach, 2003), and very high sulfide contents to precipitate elemental sulfur and to prevent gold precipitation (see Heinrich, 2005). These fluids may have their precursor in abundant superheated steam rich in CO_2, SO_2, and HCl with minor brines that discharged at shallow depth into the brittle regime, like this brecciated and altered zone (see Fournier, 1999). The numerous vapor-rich inclusions observed in quartz crystals within breccia fragments corroborates this hypothesis. These fluids could have also redissolved some copper from early stages (early Cu–Au mineralization in Trampeadero?). The various types of pyrite and the arsenopyrite and pyrite rimming early pyrite cores at these depths, is indicative of multiple fluid generation events.

At shallow levels and in the matrix-supported breccia, the presence of late colloform pyrite bands, sphalerite, emplectite, aikinite, with Au and Ag, accompanied by alunite, suggests that fluids were already depleted in Cu and As and probably had lower temperatures and volatiles (due to meteoric water mixing? or low pressure boiling?), but still high sulfur and/or low pH to precipitated alunite (Stoffregen, 1987). The various bands of colloform pyrite enriched in Zn, Cu and minor Sn, Sb, As, and Ag rimming early pyrite cores may have precipitated in open space filled with hydrothermal fluids that fluctuated in composition and temperature. Colloform pyrite bands are spatially coincidental with the polymetallic zinc (sphalerite), lead (aikinite), bismuth (emplectite) mineralization and also with zones enriched in Au and Ag, but paragenetic relations among these ore minerals themselves are not well defined. At AR-82 94 m elevation, a sphalerite veinlet cut the mineralized breccia and, also at greater depths, there are fault zones enriched in Zn that contain exceptional Pb, and do not contain Au and Ag as observed at higher structural levels (Figs. 3 and 5), consistent with most epithermal metal zonation patterns. Thus, sphalerite (sometimes galena) predates or postdated Au–Ag mineralization. Considering that sulfosalt (such aikinite and emplectite) fill voids or overgrow and (or) replace (rim) early pyrite (Fig. 14), and native gold occurs in fractures in quartz fragments, it is more likely that these minerals precipitated contemporaneous with colloform pyrite bands (Fig. 14) and fine-grained pyrite crystals in veinlets. Other Au-rich zones occur in the Trampeadero breccia and altered porphyry intersected by drill hole AR18 (Figs. 5 and 11). In this case invisible gold may be volumetrically significant: Au in late pyrite (in veinlets) reaches 600 ppm (AR-18 85 m) and up to 1000 ppm in covellite grains (AR-18 266 m) (Table 4).

10.1. Comparison to other high sulfidation epithermal environments

In the Agua Rica epithermal stage, Cu–Fe–As–Sn sulfides, diaspore, zunyite, and alunite were synchronous. In most high sulfidation systems, the copper–gold mineralization post-dates the formation of advanced argillic alteration (Stoffregen, 1987; Arribas, 1995; Gray and Coolbaugh, 1994; Hedenquist et al., 1998). In other deposits like La Pepa, gold–enargite–barite ore and quartz–alunite envelopes formed at the same time from a late supercritical magmatic fluid that cooled below its critical temperature and boiled upon ascent (Muntean and Einaudi, 2001). Epithermal veins at La Mejicana and La Rioja, Argentina (Losada-Calderón and McPhail, 1996), the epithermal, precious metal-bearing pyrite and enargite at Pascua–Lama of Chile and Argentina (Chouinard et al., 2005), the banded enargite veins at El Indio (Jannas et al., 1999), and breccia- and vein-hosted mineralization at Tambo (Jannas et al., 1999), are other examples, whereas it has been documented that alunite gangue forms with mineralization. Unlike many high sulfidation deposits (La Mejicana, Losada-Calderón and McPhail, 1996; Lepanto, Hedenquist et al., 1998; El Indio, Jannas et al., 1999; Lahóca, Gatter et al., 1999), in Agua Rica hypogene covellite is the most important copper sulfide that precipitated at intermediate depths in the advanced argillic assemblage and as replacements of early sulfides at greater depth, in equilibrium with phyllic alteration.

At Agua Rica, Au and Ag mineralization occurs at shallow levels with Bi and Pb sulfosalts accompanied by alunite, in zones depleted in Cu and As. This is similar to other high-sulfidation deposits in which gold enrichment is in late-stage veining, open-space and breccias, and post-date enargite precipitation (Nansatsu, Hedenquist et al., 1994; Rodalquilar, Arribas et al., 1995; Lepanto, Hedenquist et al., 1998; El Indio, Jannas et al., 1999). In the high sulfidation Pascua–Lama deposit of Chile and Argentina, main stage gold–silver mineralization is associated with pyrite and enargite (Chouinard et al., 2005).

10.2. Some considerations about temperature

Based on preliminary microthermometric FI data, porphyry-style alteration and mineralization was produced between 375 and >500 °C, by hypersaline fluids (and vapor) with intermediate S fugacity according to the dominant sulfides mineralogy (mainly pyrite + chalcopyrite; Fig. 15). This temperature range is similar to the temperature ranges obtained from fluid inclusions studies at the South Lepanto porphyry Cu–Au deposit (Hedenquist et al., 1998) and from Bajo de la Alumbrera (Ulrich and Heinrich, 2001). The assemblage pyrite + Cu sulfides + dioctahedral white micas + quartz + rutile or anatase of the phyllic zone suggests temperatures ≥360 °C (Fig. 15). The replacement of chalcopyrite ± bornite by covellite suggests temperatures ≤360 °C and high sulfur fugacity in the hydrothermal fluids (Einaudi et al., 2003) (Fig. 15).

The high-temperature advanced argillic alteration assemblage andalusite ± pyrite ± quartz preserved in the roots of the argillic halo and in clasts of hydrothermal breccias in the center and east sector of the section, may have been formed at temperatures ≥375 °C (cf. Hemley et al., 1980) from condensed magmatic vapor; the observed replacement of andalusite by white mica suggests a decrease in temperature rather than an increase of the K/H of hydrothermal fluids. At shallower depths, pyrophyllite replaces white micas, suggesting temperatures of formation between 280 and 360 °C. Clasts of vuggy silica in the uppermost levels of the central breccia, indicates that at lower temperatures (<250 °C) fluids reached very low pH (pH<2; Stoffregen, 1987).

Post-brecciation, intermediate temperature advanced argillic paragenesis (alunite + diaspore + zunyite + svanbergite + woodhouseite) as cement accompanied by abundant covellite, pyrite, enargite, and native sulfur (kuramite) in deepest parts of breccias indicates temperatures near 300 °C and hydrothermal fluids with high sulfur fugacity (Einaudi et al., 2003). The zunyite enriched in F also indicates the proximity to the source of a more felsic intrusion, hydrothermal fluids with significant component of magmatic volatiles (Corbett and Leach, 1998) and temperatures of formation higher than 250 °C (Reyes, 1990).

Multiple generations of pyrite, emplectite, colucite, Pb, Ag, and Bi-bearing sulfosalts, and native sulfur with Au and Ag accompanied by alunite introduction in the upper level breccias, probably occurred at lower temperatures, but still high sulfur and oxygen activity. Likewise, still high sulfur and (or) oxygen activity is indicated by the absence to very low Fe (0.00 to 0.5% Fe) in the sphalerite (Czamanske, 1974).

Veinlets of alunite with woodhouseite + svanvergite + pyrite + enargite cutting the phyllic halo suggests temperatures ~250 °C and without APS, temperatures ~200 °C (Watanabe and Hedenquist, 2001). The passage from woodhouseite–svanbergite solid solution series into alunite, reflects not only a drop in the temperature, but also a drop in the pH of the hydrothermal fluids (Watanabe and Hedenquist, 2001). Kaolinite occurs in the phyllic halo as late mineral in clots or in veinlets thus, in this zone, fluid cooled enough for its formation (<200 °C; Reyes, 1990).

11. Conclusions

This study presents the first complete cross-section analysis using drill core and drill core assay data for the Agua Rica deposit. The distribution of the hydrothermal alteration and mineralization along this key east–west section through the main part of deposit is supported by detail mineralogical data, and establish a well constrained time–space framework for the porphyry–epithermal transition at Agua Rica.

During the porphyry's emplacement stage, early potassic alteration in the Seca Norte porphyry correlates with moderate hypogene Cu and Au grades, whereas pervasive phyllic alteration in the Trampeadero and metasedimentary rock is Mo-rich and Cu- and Au-depleted. In this phyllic envelope, early stockwork veinlets preserve the textural record of dissolution of ore minerals and early chalcopyrite (bornite) and iron oxides have been reconstituted into a covellite and pyrite assemblage by late high sulfidation stages.

An early stage of advanced argillic alteration produced andalusite or andalusite ± pyrite ± quartz lenses at depth and pyrophyllite at higher elevations replacing white micas from the phyllic assemblage, and leached all previous alteration minerals leaving vuggy quartz in the upper part of the section. This stage was barren and probably originated during the absorption of early spent porphyry ore fluids that expanded to a low-density vapor.

Multistage of advanced argillic alteration and mineralization as is indicated by breccia in breccia textures and several pyrite and alunite generations, followed a new shallowly emplaced magma and the formation of interfingering granite and hydrothermal heterolithic and monolithic breccias. Fe–Cu–As–(Sn)-bearing sulfides precipitated as cement in clast-supported hydrothermal breccias at intermediate depth and in lateral transition zones to fractured and altered rocks accompanied by alunite (svanbergite ± woodhouseite), diaspore, and zunyite. These zones contains the highest grades of Cu, part of it could have been dissolved from early sulfide stages.

At shallower depths, Fe–Zn-bearing sulfides, and Pb–Bi–Cu sulfosalts with alunite are spatial coincident with Au- and Ag-rich zones of the matrix-supported heterolithic breccia. Other Au-rich zones in the section occur in shallow samples of the Trampeadero monolithic breccia with late pyrite veinlets or in deeper samples with gold-rich covellite. Zinc, and to a much lesser extent Pb mineralization, advanced downwards, controlled by fractures and overprinting much of the previous mineralization, but without Au, Ag, and Bi–Pb sulfosalts. Thus, Zn and Pb (as galena) represent an independent mineralization stage.

The Agua Rica system is characterized by the episodic superposition of multiple igneous and consequently related hydrothermal and breccia events in a subvolcanic setting undergoing exhumation during crustal denudation. Each intrusion supplied its own magmatic fluid pulse, which coalesced into a Cu–Mo–Au–Zn–Pb ore shell.

Acknowledgments

This work forms part of a project financed by Instituto de Recursos Minerales (INREMI), Consejo Nacional de Investigaciones Científicas y Técnicas Argentino (CONICET; PIP n° 6043 and 1083), and Facultad de Ingeniería de la Universidad Nacional del Comahue (PIP N° 072). We would like to thank Dr. Pablo Marcet, and Dr. J. L. Martín, managers of the Agua Rica Mining Company, for allowing us to collect samples for this study and consult unpublished reports from the Agua Rica project. We are especially grateful to Lic. Claudio Devaux, Lic. Pedro Ruiz and their assistants in Andalgalá, and to Lic. López and Lic. Gobbo for their help in the field. We also thank the support of Project PPM 00539-09 (FAPEMIG, Brazil) and Project 302683/2008-9 (CNPQ, Brazil), the Director and personnel of the Centro de Desenvolvimiento de Tecnología Nuclear (CDTN/CNEN, Brazil) for the fluid inclusion analyses, and Luis García from the Laboratorio de Microanálises del Departamento de Física, UFMG, Brazil, for the microprobe analyses. D. Lentz is supported by a NSERC Discovery grant.

References

Allmendinger, R.W., 1986. Tectonic development, southeastern border of the Puna Plateau. Geol. Soc. Am. Bull. 97, 1070–1082.

Arribas Jr., A., 1995. Characteristics of high-sulfidation epithermal deposits, and their relation to magmatic fluid. Mineral. Assoc. Can. Short Course Ser. 23, 419–454.

Arribas Jr., A., Cunningham, C.G., Rytuba, J.J., Rye, R.O., Kelly, W.C., Podwysocki, M.H., McKee, E.H., Tosdal, R.M., 1995. Geology, geochronology, fluid inclusions, and isotope geochemistry of the Rodalquilar gold-alunite deposit, Spain. Econ. Geol. 90, 795–822.

Baker, E.M., Kirwin, D.J., Taylor, R.G., 1986. Hydrothermal breccia pipes. Contributions of the Economic Geology Research Unit, Geology Department James Cook University of North Queensland: Economic Geology Research Unit Contribution, 12. 45 pp.

BHP, 1999. The Agua Rica porphyry Cu–Mo–Au deposit, Catamarca. Geology and Mineral Resource Update. Internal report. 420 pp.

Bissig, T., Lee, J.K.W., Clark, A.H., Heather, K.B., 2001. The Cenozoic history of volcanism and hydrothermal alteration in the central Andean flat-slab region: new ^{40}Ar–^{39}Ar constraints from the El Indio-Pascua Au (Ag, Cu) belt, 29° 20′–30° 30′ S. Int. Geol. Rev. 43, 312–340.

Bissig, T., Clark, A., Lee, J., Hodgson, C.J., 2002. Miocene landscape evolution and geomorphologic controls on epithermal processes in the El Indio–Pascua Au–Ag–Cu Belt, Chile and Argentina. Econ. Geol. 97, 971–996.

Burnham, C.W., 1985. Energy release in subvolcanic environments; implications for breccia formation. Econ. Geol. 80, 1515–1522.

Caelles, J.C., Clark, A.H., Farrar, E., McBride, S.L., Quirt, S., 1971. Potassium–argon ages of porphyry copper deposits and associated rocks in the Farallón Negro-Capillitas district, Catamarca, Argentina. Econ. Geol. 66, 961–964.

Candela, P.A., Holland, H.D., 1986. A mass transfer model for copper and molybdenum magmatic hydrothermal systems: the origin porphyry-type ore deposits. Econ. Geol. 81, 1–19.

Cao, X., 1989. Solubility of molybdenite and the transport of molybdenum in hydrothermal solutions. PhD Dissertation, Iowa State University, U.S.A., 111 pp.

Chouinard, A., Williams-Jones, A.E., Leonardson, R.W., Hodgson, C.J., Silva, P., Téllez, C., Vega, J., Rojas, F., 2005. Geology and genesis of the multistage high-sulfidation epithermal Pascua Au–Ag–Cu deposit, Chile and Argentina. Econ. Geol. 100, 463–490.

Clark, A.H., Farrar, E., Caelles, J.C., Haynes, S.J., Lortie, R.B., McBride, S.L., Quirt, G.S., Robertson, R.C., Zentilli, M., 1976. Longitudinal variations in the metallogenetic evolution of the central Andes; a progress report. In: Strong, D.F. (Ed.), Metallogeny and Plate Tectonics: Geological Association of Canada, Special Paper, 14, pp. 23–58.

Cline, J.S., 1995. Genesis of porphyry copper deposits: the behavior of water, chloride, and copper in crystalline melts. Ariz. Geol. Soc. Dig. 20, 69–82.

Corbett, G.J., Leach, T.M., 1998. Southwest Pacific Rim gold–copper systems; structure, alteration, and mineralization. Soc. Econ. Geol. Spec. Publ. 6 237 pp.

Czamanske, G.K., 1974. The FeS content of sphalerite along the chalcopyrite–pyrite–bornite sulfur fugacity buffer. Econ. Geol. 69, 1328–1334.

Deer, W.A., Howie, R.A., Zussman, J., 1966. An Introduction to the Rock Forming Minerals. Longman Group Limited, London, U.K.. 519 pp.

Einaudi, M.T., Hedenquist, J.W., Inan, E., 2003. Sulfidation state of hydrothermal fluids: the porphyry–epithermal transition and beyond. In: Simmons, S.F., Graham, I.J. (Eds.), Volcanic, Geothermal and Ore-Forming Fluids: Rulers and Witnesses of Processes Within the Earth: Society of Economic Geologists and Geochemical Society, Special Publication, 10, pp. 285–313.

Fournier, R.O., 1999. Hydrothermal processes related to movement of fluid from plastic into brittle rock in the magmatic–epithermal environment. Econ. Geol. 94, 1193–1211.

Gatter, I., Molnar, F., Foldessy, J., Zelenka, T., Kiss, J., Szebenyi, G., 1999. High-and low-sulfidation epithermal mineralization of the Marta Mountains, Northeast Hungary. In: Molnar, F., Lexa, J., Hedenquist, J.W. (Eds.), Epithermal Mineralization of the Western Carpathians: Society of Economic Geologists, Guidebook Series, 31, pp. 155–179.

Giggenbach, W.F., 2003. Magma degassing and mineral deposition in hydrothermal systems along convergent plate boundaries. Soc. Econ. Geol. Spec. Publ. 10, 1–18.

Gray, J.F., Coolbaugh, M.F., 1994. Geology and geochemistry of Summitville, Colorado: an epithermal acid-sulfate deposit in a volcanic dome. Econ. Geol. 89, 1906–1923.

Gu, Y., 1993. Theoretical and experimental studies of the hydrothermal geochemistry of molybdenum. Unpublished Ph.D. thesis, Monash University, Melbourne, Australia, 177 pp.

Gustafson, L.B., Hunt, J.P., 1975. The porphyry copper deposit at El Salvador, Chile. Econ. Geol. 70, 857–912.

Halter, W.E., Bain, N., Becker, K., Heinrich, C.A., Landtwing, M., vonQuadt, A., Clark, A., Sasso, A.M., Bissig, T., Tosdal, R.M., 2004. From andesitic volcanism to the formation of a porphyry Cu–Au mineralizing magma chamber: the Farallón Negro Volcanic Complex, northwestern Argentina. J. Volcanol. Geotherm. Res. 136, 1–30.

Halter, W.E., Heinrich, C.A., Pettke, T., 2005. Magma evolution and the formation of porphyry Cu–Au ore fluids: evidence from silicate and sulfide melt inclusions. Miner. Deposita 39, 845–863.

Harris, A., Bryan, S., Holcombe, R., 2006. Volcanic setting of the Bajo de la Alumbrera porphyry Cu–Au deposit, Farallón Negro Volcanics, Northwest Argentina. Econ. Geol. 101, 71–94.

Hedenquist, J.W., Matsuhisa, Y., Izawa, E., White, N.C., Giggenbach, W.F., Aoki, M., 1994. Geology, geochemistry, and origin of high sulfidation Cu–Au mineralization in the Nansatsu district, Japan. Econ. Geol. 89, 1–30.

Hedenquist, J.W., Arribas, A., Reynolds, T.J., 1998. Evolution of an intrusion-centered hydrothermal system: Far Southeast–Lepanto porphyry and epithermal Cu–Au deposits, Philippines. Econ. Geol. 93, 373–404.

Heinrich, C.A., 2005. The physical and chemical evolution of low-salinity magmatic fluids at the porphyry to epithermal transition: a thermodynamic study. Miner. Deposita 39, 864–889.

Hemley, J.J., Montoya, J.W., Marinenko, J.W., Luce, R.W., 1980. Equilibria in the system Al_2O_3–SiO_2–H_2O and some general implications for alteration–mineralization processes. Econ. Geol. 75, 210–228.

Jannas, R.R., Bowers, T.S., Petersen, U., Beane, R.E., 1999. High-sulfidation deposit types in the El Indio district, Chile. In: Skinner, B.J. (Ed.), Geology and Ore Deposits of the Central Andes: Society of Economic Geologists, Special Publication, 7, pp. 219–266.

Jordan, T.E., Allmendinger, R.W., 1986. The Sierra Pampeanas of Argentina: a modern analog of Rocky Mountain foreland deformation. Am. J. Sci. 286, 737–764.

Kesler, S.E., Wilkinson, B.H., 2006. The role of exumation in the temporal distribution of ore deposits. Econ. Geol. 101, 919–922.

Klemm, L.M., Pettke, T., Heinrich, C., 2008. Fluid and source magma evolution of the Questa porphyry Mo deposit, New Mexico, USA. Miner. Deposita 43, 533–552.

Koukharsky, M., Mirré, J.C., 1976. Mi Vida prospect: a porphyry copper-type deposit in northwestern Argentina. Econ. Geol. 71, 849–863.

Landtwing, M., 1998. Breccias in the Cu–Mo–Au prospect of Agua Rica, Argentina: Evolution of a magmatic–hydrothermal system during progressive unroofing. Unpublished diploma thesis, ETH Zürich, Switzerland, 60 pp..

Landtwing, M., Dillenbeck, E., Leake, M., Heinrich, C., 2002. Evolution of the breccia-hosted porphyry-Cu–Mo–Au deposit at Agua Rica, Argentina: progressive unroofing of a magmatic–hydrothermal system. Econ. Geol. 97, 1273–1292.

Llambías, E.J., 1970. Geología de los Yacimientos Mineros Agua de Dionisio, Provincia de Catamarca, República Argentina. Rev. Asoc. Argent. Mineral. Petrol. Sedimentol. 1, 2–32.

Llambías, E.J., 1972. Estructura del Grupo Volcánico Farellón Negro, Catamarca, República Argentina. Rev. Asoc. Geol. Argent. 2, 161–169.

Losada-Calderón, A.J., McPhail, F.C., 1996. Porphyry and high-sulfidation epithermal mineralization in the Nevados del Famatina mining district, Argentina. In: Camus, F., Sillitoe, R.H., Petersen, R. (Eds.), Society of Economic Geology Special Publication, 5, pp. 91–117.

Malvicini, L., Llambías, E., 1963. Mineralogía y origen de los minerales de manganeso y sus asociados en Farallón Negro, Alto de la Blenda y Los Viscos, Hualfín, Catamarca. Rev. Asoc. Geol. Argent. 18, 177–200.

Márquez-Zavalía, M.F., 1999. El yacimiento Capillitas, provincia de Catamarca. In: Zappettini, E.O. (Ed.), Recursos Minerales de la República Argentina: Instituto de Minería y Recursos Minerales, Buenos Aires. Anales, 35, pp. 1643–1652.

Márquez-Zavalía, M.F., Craig, J.R., 2004. Tellurium and precious-metal ore minerals at Mina Capillitas, Northwestern Argentina. Neues Jahrb. Mineral. Monatsh. 176–192.

Moore, D.M., Reynolds, R.J.R., 1997. X-Ray Diffraction and the Identification and Analysis of Clay Minerals. Oxford University Press, New York. 378 pp.

Munoz, J.L., 1984. F–OH and Cl–OH exchange in micas with applications to hydrothermal ore deposits. In: Bailey, S.W. (Ed.), Micas: Reviews in Mineralogy, 13, pp. 469–494.

Muntean, J.L., Einaudi, M.T., 2001. Porphyry–epithermal transition: Maricunga Belt, northern Chile. Econ. Geol. 96, 743–772.

Navarro, H., 1986. Geología general y económica del pórfido de cobre-molibdeno “Mi Vida”, Andalgalá, Catamarca. Rev. Inst. Geol. Univ. Nac. Jujuy 6, 127–154.

Newman, A., Brown, G., 1987. The chemical constitution of Clays. In: Newman, A. (Ed.), Chemistry of Clays and Clay Minerals: Mineralogical Society Monograph, 6. 129 pp.

Perelló, J., Rojas, N., Devaux, C., Fava, L., Etchart, E., Harman, P., 1998. Discovery of the Agua Rica porphyry Cu–Mo–Au deposit, Catamarca Province, northwestern Argentina, part II: geology. In: Porter, T.M. (Ed.), Porphyry and hydrothermal copper and gold deposits, a global perspective: Glenside, South Australia, Australian Mineral Foundation, Symposium, Perth, W.A. , pp. 117–132.

Perry, W.T., Jasumback, M., Wilson, P.N., 2002. Clay mineralogy of phyllic and intermediate argillic alteration at Bingham, Utah. Econ. Geol. 97, 221–239.

Proffett, J.M., 2003. Geology of the Bajo de la Alumbrera porphyry copper–gold deposit, Argentina. Econ. Geol. 98, 1535–1574.

Redmond, P.B., Einaudi, M.T., Inan, E.E., Landtwing, M.R., Heinrich, C.A., 2004. Copper deposition by fluid cooling in intrusion-centered systems: new insights from the Bingham porphyry ore deposit, Utah. Geology 32, 217–220.

Reyes, A.G., 1990. Petrology of Philippine geothermal systems and the application of alteration mineralogy to their assessment. J. Volcanol. Geotherm. Res. 43, 279–309.

Rios, F.J., Alves, J.V., Perez, C., Costa, E.C., Rosiére, C.A., Fuzikawa, K., Correia Neves, J.M., Chaves, A.O., Prates, S., De Barrio, R., 2006. Combined investigations of fluid inclusions in opaque ore minerals by NIR/SWIR microscopy and microthermometry and Synchrotron Radiation X-ray fluorescence. Special issue Frontiers in analytical geochemistry. Appl. Geochem. 21, 813–819.

Robb, L., 2005. Introduction to Ore-forming Processes. Blackwell Publishing, Oxford, U.K.. 373 pp.

Rohrlach, B.D., 2003. Tectonic evolution, petrochemistry, geochronology and palaeohydrology of the Tampakan Porphyry and high-sulfidation epithermal Cu–Au deposit, Mindanao, Philippines. Unpublished Ph.D. thesis, Australian National University, Canberra, 499 pp + appendices.

Rojas, N., Perelló, J., Harman, P., Cabello, J., Devaux, C., Fava, L., Etchart, E., 1998. Discovery of the Agua Rica porphyry Cu–Mo–Au deposit, Catamarca Province, northwestern Argentina, part I: exploration and discovery. In: Porter, T.M. (Ed.), Porphyry and hydrothermal copper and gold deposits, a global perspective: Glenside, South Australia, Australian Mineral Foundation, Symposium, Perth, Western Australia, pp. 111–117.

Ronacher, E., Richards, J.P., Reed, M.H., Bray, C.J.E., Spooner, T.C., Adams, P.D., 2004. Characteristics and evolution of the hydrothermal fluid in the north zone high-grade area, Porgera Gold Deposit, Papua New Guinea. Econ. Geol. 99, 843–867.

Rosco, R., Koukharsky, M., 1999. El pórfiro cupro-molibdenífero Agua Rica y las manifestaciones epitermales asociadas, Catamarca. In: Zappettini, E. (Ed.), Recursos Minerales de la República Argentina: Instituto de Geología y Recursos Minerales, Buenos Aires, Anales, 35, pp. 1479–1492.

Rosiére, C.A., Rios, F.J., 2004. The origin of hematite in high grade iron ores based on infrared microscopy and fluid inclusion studies. The example of the Conceição Mine, Quadrilatero Ferrifero, Brazil. Econ. Geol. 99, 611–624.

Rusk, B., Reed, M., Dilles, J., 2008. Fluid Inclusions evidence for magmatic–hydrothermal fluid evolution in the porphyry copper–molybdenum deposit at Butte, Montana. Econ. Geol. 103, 307–334.

Sasso, A.M., 1997. Geological evolution and metallogenetic relationships of the Farallón Negro volcanic complex, NW Argentina. Unpublished Ph.D. thesis, Queen's University, Kingston, Ontario, 843 pp.

Sasso, A.M., Clark, A.H., 1998. Magmatic, hydrothermal and tectonic evolution and implications for Cu–Au metallogeny in the Andean back-arc. Soc. Econ. Geol. (SEG) Newsl. 34 (1), 8–17.

Seedorff, E., Einaudi, M., 2004. Henderson Porphyry Mo System, Colorado: I. Sequence and abundance of hydrothermal mineral assemblages, flow paths and evolving fluids and evolutionary style. Econ. Geol. 99, 3–37.

Selby, D., Nesbitt, B.E., 2000. Chemical composition of biotite from the Casino porphyry Cu–Au–Mo mineralization, Yukon, Canada: evaluation of magmatic and hydrothermal fluid chemistry. Chem. Geol. 171, 77–93.

Sillitoe, R.H., 1985. Ore-related breccias in volcanoplutonic arcs. Econ. Geol. 80, 1467–1514.

Stemprok, M., 1990. Solubility of tin, tungsten, and molybdenum in felsic magmas. Miner. Deposita 25, 205–212.

Stoffregen, R.E., 1987. Genesis of acid-sulfate alteration and Au–Cu–Ag mineralization at Summitville, Colorado. Econ. Geol. 82, 1575–1591.

Stoffregen, R.E., Alpers, C.N., 1987. Woodhouseite and svanbergite in hydrothermal ore deposits: products of apatite destruction during advanced argillic alteration. Can. Mineral. 25, 201–211.

Tingle, T.N., Fenn, P.M., 1984. Transport and concentration of molybdenum in granite molybdenite systems: effects of fluorine and sulfur. Geology 12, 156–158.

Ulrich, T., Heinrich, C.A., 2001. Geology and alteration geochemistry of the porphyry Cu–Au deposit at Bajo de la Alumbrera, Argentina. Econ. Geol. 96, 1719–1742.

Ulrich, T., Mavrogenes, J., 2008. An experimental study of the solubility of molybdenum in H_2O and KCl–H_2O solutions from 500 °C to 800 °C, and 150 to 300 MPa. Geochim. Cosmochim. Acta 72, 2316–2330.

Ulrich, T., Günther, D., Heinrich, C.A., 2001. The evolution of a porphyry Cu–Au deposit, based on LA-ICPMS analysis of fluid inclusions: Bajo de la Alumbrera, Argentina. Econ. Geol. 96, 1743–1774.

Urreiztieta, M., Rosello, E.A., Gapais, D., LeGorve, C., Cobbold, P.R., 1993. Neogene dextural transpression at the southern edge of the Altiplano–Puna (NW Argentina). II International Symposium on Andean Tectonics, Oxford. Editions de l'Office de la Recherche Scientifique et Technique d'Outre-mer, Paris, pp. 267–269.

Watanabe, Y., Hedenquist, J.W., 2001. Mineralogical and stable isotope zonation at the surface over the El Salvador porphyry Cu deposit, Chile. Econ. Geol. 96, 1775–1797.

William-Jones, A., Heinrich, C.A., 2005. Vapor transport and the formation of magmatic–hydrothermal ore deposits. Econ. Geol. 100, 1287–1312.

Wood, S.A., Crerar, D.A., Borcsik, M.P., 1987. Solubility of the assemblage pyrite–pyrrhotite–magnetite–sphalerite–galena–Au–stibnite–bismuthinite–argentite–molybdenite in H_2O–CO_2–NaCl solutions from 200 °C to 350 °C. Econ. Geol. 82, 1864–1887.

Woodcock, J.R., Hollister, V.F., 1978. Porphyry molybdenite deposits of the North American Cordillera. Miner. Sci. Eng. 10, 3–18.